Tracer Simulation Using a Global General Circulation Model: Results from a Midlatitude Instantaneous Source Experiment

J. D. MAHLMAN AND W. J. MOXIM

Geophysical Fluid Dynamics Laboratory, NOAA, Princeton University, Princeton, NJ. 08540

(Manuscript received 22 November 1977, in final form 13 April 1978)

ABSTRACT

An 11-level general circulation model with seasonal variation is used to perform an experiment on the dispersion of passive tracers. Specially constructed time-dependent winds from this model are used as input to a separate tracer model. The methodologies employed to construct the tracer model are described.

The experiment presented is the evolution of a hypothetical instantaneous source of tracer on 1 January with maximum initial concentration at 65 mb, 36°N, 180°E. The tracer is assumed to have no sources or sinks in the stratosphere, but is subject to removal processes in the lower troposphere.

The experimental results reveal a number of similarities to observed tracer behavior, including the average poleward-downward slope of mixing ratio isopleths, strong tracer gradients across the tropopause, intrusion of tracer into the Southern Hemisphere lower stratosphere, and the long-term interhemispheric exchange rate. The model residence times show behavior intermediate to those exhibited for particulate radioactive debris and gaseous $C^{14}O_2$. This suggests that caution should be employed when either radioactive debris or $C^{14}O_2$ data are used to develop empirical models for prediction of gaseous tracers which are efficiently removed in the troposphere.

In this experiment, the tracer mixing ratio and potential vorticity evolve to very high correlations. Mechanisms for this correlation are discussed. The zonal mean tracer balances exhibit complex behavior among the various transport terms. At early stages, the tracer evolution is dominated by eddy effects. Later, a very large degree of self-cancellation between mean cell and eddy effects is observed. During seasonal transitions, however, this self-cancellation diminishes markedly, leading to significant changes in the zonal mean tracer distribution. A possible theoretical explanation is presented.

For this tracer dispersion problem, probably the most significant model shortcoming is the inability of the general circulation model to produce the midwinter stratospheric sudden warming phenomenon.

1. Introduction

The transport and behavior of trace constituents in the stratosphere has been a subject of great interest for a number of years. Originally, the effort was directed toward the attempt to understand why the observed distribution of ozone is so remarkably unlike that which would be expected if its distribution were under photochemical control (e.g., Craig, 1950). Later, the behavior of debris from nuclear weapons tests became a subject of concern. This was particularly the case when it was observed that radioactive debris returned from the stratosphere at a rate appreciably faster and more selectively than had been originally anticipated.

In addition, it was found that the trace constituent measurements revealed a number of features which were not readily explainable in terms of current understanding of atmospheric behavior. These included the poleward-downward slope of mixing ratio isolines in the lower stratosphere, the midlatitude peak of radioactivity in the troposphere, and the spring maximum and fall minimum of concentration in the troposphere. Although progress has been made by a large number of investigators toward understanding these phenomena, there do not yet exist completely satisfactory quantitative theories for explaining any of them.

Problems of this type have stimulated considerable research on improving basic knowledge of the joint stratosphere-troposphere system. It has become clear that in order to claim complete understanding of tracer behavior, it is necessary to possess a strong understanding of the dynamical climatology of this part of the atmosphere. In addition, it is necessary that this understanding be interpreted properly in terms of the mechanisms which are responsible for controlling the dispersion of trace constituents on a global scale. In some cases, however, the problem is made even more complex because the radiative-dynamical structure (and thus the tracer transport) is in part determined by the manner in which trace constituents are transported in the system. The two most prominent examples of this are water vapor and ozone.

In the research reported here, the emphasis is on the behavior of passive tracers, i.e., ones that have no feed-

back to the transporting winds. Through use of a numerical general circulation model (GCM), the transporting winds (on the presumably important scales) are calculated explicitly as a function of time over the entire globe. To the degree currently possible, every effort has been made in the GCM to obtain the model climatology using basic physical laws with a minimum of ad hoc tuning to force model agreement with observation.

Such an approach strongly demands that the model-simulated processes be sufficiently similar to those occurring in the actual atmosphere that the dispersion of tracers is also close to that observed. Once these constraints have been satisfactorily met, analysis of the model atmosphere can often yield improved insights into the processes occurring in the actual atmosphere.

Before proceeding further, it is useful to review some of the previous thinking as to what types of processes have been considered to be the most important for redistributing tracers in the stratosphere. The earliest school of thought centered around the concept of the stratosphere being dominated by a large meridional circulation with rising motion near the equator, poleward movement in the middle stratosphere, and sinking at high latitudes (Brewer, 1949). This concept was reiterated by other authors including Dobson (1956), Goldie (1958) and Libby and Palmer (1960).

On the other hand, many other investigators proposed that zonally asymmetric motions (eddies) were important for the large-scale dispersion of tracers. The importance of vertical eddy flux of ozone was proposed by Reed and Julius (1951). Later, Reed (1953) suggested that horizontal eddy flux might also be important. Similar suggestions were made by Godson (1960), Ramanathan and Kulkarni (1960) and Boville and Hare (1961) relative to the ozone transport problem. The behavior of tungsten-185 following a series of low-latitude nuclear tests in 1958 led Feely and Spar (1960) and Newell (1961) to suggest that eddy processes dominated the poleward transfer. In addition, Newell (1963) pointed out that the observed poleward-downward slope of mixing ratio isopleths is probably related to the stratosphere being a place where the kinetic energy is provided by import from the troposphere rather than *in situ* generation.

Later, a number of observational studies showed that the actual stratospheric meridional circulation is quite different from that hypothesized by Brewer (1949), particularly in higher latitudes (e.g., Reed *et al.*, 1963; Julian and Labitzke, 1965; Murakami, 1965; Mahlman, 1966, 1969a). In particular, it was noted in Mahlman (1966, 1969a) that the stratospheric heat balance is such that the heating effect of the meridional circulation acts in opposition to that produced by large-scale eddy flux convergence of heat. This led Mahlman (1966) to hypothesize that the stratospheric dispersion of trace constituents is a rather complicated function of interactive mean cell and eddy transports. This was verified in a GCM experiment by Hunt and Manabe (1968). Their results from an annual mean model showed the presence of a large degree of cancellation between mean cell and eddy effects in the dispersion of passive tracers.

A related problem which has also commanded a great deal of attention is that of the processes responsible for the transport of tracers between the stratosphere and troposphere. The meridional circulation hypothesized by Brewer (1949) was visualized as a way of explaining the extreme dryness of the lower stratosphere. However, it was soon realized that the return of radioactivity from the stratosphere appeared to be quite variable and mainly confined to midlatitudes. This observation was seen to be compatible with the demonstrations of Reed and Sanders (1953) that significant amounts of stratospheric air can enter the troposphere in the intense baroclinic zone below the polar front jet stream to the west of extratropical cyclones. This was verified in subsequent case studies by Reed (1955), Reed and Danielsen (1959), Danielsen (1959a,b) and Staley (1960). The events were shown to be associated with high radioactivity values by Staley (1962), Reiter (1963), Danielsen (1964, 1968), Mahlman (1965) and Reiter and Mahlman (1965). Also Danielsen (1964) and Mahlman (1965) showed that this descent of stratospheric air into the troposphere occurs in association with cyclogenesis in the upper troposphere. In addition, a direct relationship of this process to the total input of stratospheric air into the midlatitude troposphere was demonstrated statistically by Mahlman (1966, 1969b).

This point was made somewhat more quantitative by Kida (1977a,b) in a Lagrangian analysis of a simplified GCM. His result indicated that the baroclinic process of cyclogenesis and its concomitant lowering of the center of mass leads to a systematic downward flux of air in such regions. The dynamics of the actual intrusion process were put on a firmer theoretical footing by Hoskins (1971) and Mudrick (1974).

Another potentially important cross-tropopause transport mechanism is the mean circulation about local jet streams. Krishnamurti (1961a,b) showed a direct transverse circulation about the subtropical jet stream operating in the same sense as the Hadley circulation. Mahlman (1973a) demonstrated a similar effect about the polar front jet stream, but which acts opposite to the indirect Ferrel circulation operative at those latitudes.

A proper numerical simulation of tracer behavior should be able to successfully reproduce all of the important transporting phenomena. Thus, a well-posed tracer experiment can provide an excellent test of the validity of a GCM. Furthermore, it allows an examination of various simulated transport phenomena as they interact with each other.

The tracer model described in this paper is being

applied to a number of diverse tracer problems involving stratospheric transport and chemistry. These include artificial radioactivity, ozone, nitrous oxide, total odd nitrogen and stratospheric aircraft effluent. When this work was begun, only ozone and radioactive debris offered data sufficient to allow an unbiased evaluation of the tracer model performance. Of these two, ozone is less appropriate for an initial model test because of its dependence on a very complex chemistry involving a number of trace constituents. The behavior of radioactive debris following a nuclear weapons detonation is regarded as a better subject for modeling because of the relatively simple character of its sources and sinks. In future experiments, the model strengths and weaknesses revealed in the present experiment will be used to facilitate the interpretation of results for trace constituents in which the available data base is less adequate.

For this experiment, the behavior of a simulated release of tracer into the midlatitude lower stratosphere is described. Emphasis is placed on the mechanisms responsible for the long-term, large-scale dispersion and removal of the tracer, and its relation to similar tracer events in the actual atmosphere. More detailed tracer behavior in the model will be described in future papers.

2. Brief description of the general circulation model

a. *Model structure*

The GCM used to obtain the input winds for the tracer model is a modified version of the model of Holloway and Manabe (1971). The major differences between this model and the earlier version are the incorporation of a seasonal variation and a somewhat increased vertical grid resolution.

The GCM is global in extent and includes the effects of topography and land-sea contrast. Water vapor is a prognostic variable, while ozone, cloudiness and sea surface temperature are prescribed according to their observed values. The horizontal grid spacing is about 265 km. In the vertical, 11 levels are included with spacing to resolve the structure of the stratosphere as well as the surface boundary layer. The approximate pressures and heights can be seen in Table 1 of Manabe *et al.* (1974), and in Fig. 5.1 of this paper.

Spherical coordinates are used for integration of the hydrostatic "primitive" equations of motion, the first law of thermodynamics, and the equations of continuity of mass and water vapor. The vertical coordinate is the so-called "sigma" system of Phillips (1957) under the assumption of vanishing vertical sigma velocity at the top and bottom of the atmosphere. The finite-differencing system is very similar to that proposed by Kurihara and Holloway (1967). The effects of subgrid-scale mixing are approximated by the nonlinear viscosity formulation of Smagorinsky (1963). In the vertical direction, subgrid-scale mixing is applied only in the surface boundary layer according to a mixing-length hypothesis.

The method used for computing radiative transfer is the same as described by Manabe and Strickler (1964) and Manabe and Wetherald (1967). The insolation at the top of the atmosphere is dependent on latitude, season and solar distance, while the diurnal cycle is eliminated. The prescribed clouds are a function of latitude and height, but not of season and longitude. Carbon dioxide is set to a volume mixing ratio of 300 parts per million everywhere. The prescribed ozone is a function of latitude, height and season, but not of longitude. The ozonesonde data of Hering and Borden (1964) are used, and the Southern Hemisphere values are assumed to be a mirror image of the values used for the analogous season in the Northern Hemisphere.

The scheme for including the subgrid-scale effects of moist convection is the so-called "moist convective adjustment" of Manabe *et al.* (1965). The surface heat balance and hydrologic processes are the same as given in Holloway and Manabe (1971).

b. *Some pertinent model results*

Due to the magnitude and scope of the results obtained in this GCM experiment, a number of studies have already been published on various aspects of the meteorological behavior of the model (e.g., Mahlman, 1973a; Hayashi, 1974; Manabe *et al.*, 1974; Hahn and Manabe, 1975; Manabe and Holloway, 1975; Manabe and Mahlman, 1976; Hayashi and Golder, 1977). For details of the model simulation, the reader is referred to these papers. The model results most pertinent to this work are contained in the stratospheric analysis paper of Manabe and Mahlman (1976), hereafter referred to as MM76.

In the interest of brevity, the model features most clearly related to the tracer problem are presented in capsule form in Table 1. In this table, the less than successful parts of the GCM simulation are stressed to acquaint the reader with possible distortions in interpretation of the tracer results. For much greater detail on the model results, the reader is referred to the papers listed above.

3. Basic tracer model structure

a. *Processing of the basic data*

In a fundamental model calculation involving a tracer which is completely passive (no influence on the advecting wind field), an investigator has two choices: either an additional dependent variable can be included as the basic calculation is performed, or the model-determined, time-dependent winds can be stored "off-line" on computer tapes for subsequent experiments with an independent model designed for the passive tracer problem. ("Off-line" means that information is taken from the GCM and used in a different model.)

TABLE 1. Capsule review of pertinent simulation results from the GCM used for this study.

Category	Comments
Zonal mean temperature	Very good below 38 mb. Too cold in polar night middle stratosphere by 20 K. Northern Hemisphere (N.H.) midwinter stratospheric warming not simulated.
Tropopause	Agrees well with observed poleward-downward slopes and appears at the proper altitudes.
Zonal mean wind	N.H. subtropical jet slightly weaker than observed. Polar night stratospheric jet too strong by a factor of 2. Tropical stratospheric easterlies too strong by 15 m s^{-1}; quasi-biennial oscillation not simulated. Seasonal variation of zonal wind qualitatively satisfactory.
Meridional circulation	Qualitatively correct: 3-cell troposphere, 2-cell N.H. stratosphere, 3-cell S.H. stratosphere. Midstratosphere flow from summer to winter hemisphere.
Eddy kinetic energy	Somewhat too small in midlatitude troposphere. Good in N.H. stratosphere. Very large seasonal and interhemispheric variations in stratosphere.
Stationary disturbances	Structure very good, amplitude somewhat large, particularly in N.H. middle stratosphere winter.
Transient disturbances	Cyclonic disturbances somewhat weak in midlatitude troposphere. Transient long waves somewhat weak in midlatitude stratosphere. Tropical transient waves qualitatively correct but vortex disturbances too large in scale.
Precipitation	General qualitative agreement with observation. Average continental precipitation somewhat too high. Too little precipitation in southern United States and southwestern China.

The off-line approach is used for the experiments described here.

The method of adding an extra dependent variable in the GCM was employed in the tracer studies by Hunt and Manabe (1968) and Hunt (1969), using the model described by Manabe and Hunt (1968). A similar approach was used by Cunnold *et al.* (1975). The advantage of such an approach is that comparatively little additional effort is required to execute a tracer experiment once the GCM itself is ready for performing experiments. The disadvantage is that the computational expense is very large because of the necessity of reexecuting the GCM for all tracer experiments. This tends in practice to severely limit the flexibility of the investigator to perform needed intercomparison tests and checks of model deficiencies. It also acts to seriously reduce the number and length of possible tracer experiments which can be executed.

By running the tracer experiments off-line from the GCM, it is possible to design the problems with a great improvement in flexibility and computational efficiency. The increase in computational speed results mainly from avoiding the requirement of repeating the GCM integration for each tracer experiment. An additional advantage is gained because the tracer model time step can be longer than that allowed in the dynamical calculation. This is because the tracer model time step is only limited by the largest wind speed, while the GCM time step is limited in addition by the phase speed of the highest frequency disturbances generated.

A disadvantage of the off-line method is that significant effort is required to prepare a new three-dimensional model which operates independently of the GCM itself. Another difficulty with this approach involves processing of the dynamical model-generated wind fields. If all the model wind data were saved every time step, an exorbitant amount of tape storage would be required. Also, an excessive amount of computer time would be spent reading and writing tapes. On the other hand, if only a portion of the entire sequence of instantaneous data is retained, serious computational difficulties can arise. If there are any oscillations in the model whose frequencies are near to a submultiple of the sampling interval, then significant aliasing distortion can occur.

Another problem which arises in using periodic samples of GCM instantaneous data occurs when one imposes the highly desirable constraint of mass conservation on the transport terms. This can be illustrated by considering the following simple problem. If the tracer mixing ratio (R) is conserved, it is described simply by

$$\frac{dR}{dt}=0. \tag{3.1}$$

In the "sigma" coordinate system (Phillips, 1957), Eq. (3.1) can be written as

$$\frac{\partial R}{\partial t}=-\mathbf{V}_2\cdot\nabla_\sigma R-\dot{\sigma}\frac{\partial R}{\partial \sigma}, \tag{3.2}$$

where $\sigma=p/p_*$, p is pressure, p_* the surface pressure, $\mathbf{V}_2$ the horizontal wind vector, ∇_σ the gradient operator on the σ surface and $\dot{\sigma}=d\sigma/dt$ is the "vertical motion" in this coordinate system. By multiplying Eq. (3.2) by p_*, multiplying the mass continuity equation in this system

$$\frac{\partial p_*}{\partial t}=-\nabla_\sigma\cdot\mathbf{V}_2 p_*-\frac{\partial}{\partial \sigma}\dot{\sigma}p_* \tag{3.3}$$

by R, and adding the two equations together, one obtains

$$\frac{\partial Rp_*}{\partial t} = -\nabla_\sigma \cdot \mathbf{V}_2 p_* R - \frac{\partial}{\partial \sigma}\dot{\sigma} p_* R. \tag{3.4}$$

Since the ground is a coordinate surface in σ coordinates, reasonable boundary conditions in this system are $\dot{\sigma}=0$ at $\sigma=1$ and $\sigma=0$. Eq. (3.4) thus has the property upon integration over the model coordinates that

$$\frac{\partial}{\partial t}\int_M Rp_* dA d\sigma = \frac{\partial}{\partial t}\int_M R dA dp = 0. \tag{3.5}$$

Thus, no sources or sinks of tracer appear in this transport part of the calculation as long as a form similar to Eq. (3.4) is used.

However, if one attempts to integrate Eq. (3.4) numerically by interpolation between successive (say daily) instantaneous GCM information sets, one is caught in the position of extrapolating apparently large (but not actually sustained) surface pressure tendencies ($\partial p_*/\partial t$) over unrealistically long periods of time. Because the actual changes of p_* between the adjacent sampled time levels are not compatible with the computed instantaneous p_* tendencies, the large error created in the left-hand side of Eq. (3.4) will be manifested as a severe distortion in the tracer tendency itself.

One way to circumvent these difficulties in performing off-line experiments is to utilize time-averaged motion fields. If the time-averaging operator

$$\overline{(\ )}^t = \frac{1}{t_b - t_a}\int_{t_a}^{t_b} (\ )dt \equiv (\ ) - (\ )''$$

is applied over the time interval $t_b - t_a$ to Eq. (3.4), one obtains

$$\frac{\partial}{\partial t}\overline{R}^t \overline{p_*}^t = -\left[\nabla_\sigma \cdot \overline{\mathbf{V}_2 p_*}^t \overline{R}^t + \frac{\partial}{\partial \sigma}\overline{\dot{\sigma} p_*}^t \overline{R}^t\right]$$

$$-\left[\frac{\partial}{\partial t}\overline{p_*''R''}^t + \nabla_\sigma \cdot \overline{(\mathbf{V}_2 p_*)''R''}^t + \frac{\partial}{\partial \sigma}\overline{(\dot{\sigma} p_*)''R''}^t\right]. \tag{3.6}$$

The first set of terms on the right-hand side of Eq. (3.6) should correspond essentially to the effect of the meteorologically realistic motions resolved by the model. This is valid provided the averaging interval is short enough that the structure of transient disturbances remains adequately described by viewing linear interpolations between successive time-averaged states. Clearly, excessively long averaging intervals (say, a week or a month) would be inappropriate. For this study, a time-averaging interval of 6 h was chosen. With such a suitably short interval, it is reasonable to assert that no significant physical processes will be described by the second set of terms on the right-hand side of Eq. (3.6). It is possible, however, that these terms could have an effect if there are significant computational modes in the model calculation. In this case, it would be presumably better to have filtered out such nonphysical effects by utilizing only the time-averaged wind fields for the tracer calculation. However, analysis of time series using every step of the GCM shows that the contribution of frequencies shorter than 6 h is extremely small. Accordingly, in these experiments all flux divergence calculations are performed using only the first part of the right-hand side of Eq. (3.6).

b. Formulation of various tracer affecting processes

1) THE GOVERNING EQUATION

As argued in the previous section, the transport of tracer by the resolved motions in the GCM is assumed to be governed by Eq. (3.6) minus the second set of terms on its right-hand side. There are other processes which also act to affect the tracer distribution. These processes will be noted here by the following descriptive terms: "FILLING," "DIFFUSION," "SOURCES" and "SINKS." Their particular computational forms and physical interpretations will be described below. They are described in some detail because this model is being utilized for a number of tracer experiments beyond the one described here. Readers who are uninterested in such model details may skip directly to Section 4.

From the above-mentioned effects and the applicable part of Eq. (3.6), the tracer continuity equation for this study can be written symbolically as

$$\frac{\partial}{\partial t}\overline{p_*}^t \overline{R}^t = -\nabla_\sigma \cdot \overline{\mathbf{V}_2 p_*}^t \overline{R}^t - \frac{\partial}{\partial \sigma}\overline{\dot{\sigma} p_*}^t \overline{R}^t + \text{FILLING}$$

$$+\text{DIFFUSION}+\text{SOURCES}-\text{SINKS}, \tag{3.7}$$

where

$$\nabla_\sigma(\ ) = \frac{1}{a\cos\phi}\frac{\partial}{\partial \lambda_\sigma}(\ ) + \frac{1}{a\cos\phi}\frac{\partial}{\partial \phi_\sigma}[(\ )\cos\phi],$$

λ is longitude and ϕ latitude.

2) NUMERICAL EVALUATION OF FLUX DIVERGENCES

As implied in Section 3a, the explicit transport by the model-resolved, time-averaged (6 h) motions is given by the

$$\nabla_\sigma \cdot \overline{\mathbf{V}_2 p_*}^t \overline{R}^t \quad \text{and} \quad \frac{\partial}{\partial \sigma}\overline{\dot{\sigma} p_*}^t \overline{R}^t$$

terms in Eq. (3.7). If the problem has been well posed, these terms should provide the dominant contribution to the simulated tracer transport. (This does not necessarily imply that atmospheric transport should

locally dominate over SOURCES and SINKS.) The finite-difference expressions used for

$$\nabla_\sigma \cdot \overline{\overline{V_2 p_*}^{t}\overline{R}}^{t} \quad \text{and} \quad \frac{\partial}{\partial\sigma}\overline{\dot{\sigma}\overline{p_*}^{t}\overline{R}}^{t}$$

in Eq. (3.7) employ the "box" method for the irregular grid given by Kurihara and Holloway (1967). In this system, the grid "boxes" are aligned regularly in the zonal direction. However, to preserve the approximate area and shape of the boxes over the entire sphere, the box centers are not necessarily regularly aligned in the meridional direction. This necessitates evaluating flux divergences for each grid box as surface integrals by summing the local flux across the interface contiguous to the box of interest [the "key box" (0) and the adjacent box (l)]. All variables appear at the center of each grid box in the horizontal. In this spherical framework, it is convenient to define a weight w_l for each box interface as

$$w_l = \frac{d_l}{A_{\text{box}}(0)}. \tag{3.8}$$

Here d_l is the length of the common interface between the key box and the adjacent boxes; and A_{box} is the horizontal area of the key box defined as

$$A_{\text{box}} = a^2(\sin\phi_{\text{N}} - \sin\phi_{\text{S}})(\lambda_{\text{E}} - \lambda_{\text{W}}),$$

where a is the radius of the equivalent spherical earth and N, S, E and W stand for the directions toward the respective edges of the box. Note that $w_l = 1/\Delta x$ in a regular Cartesian grid where $\Delta x = \Delta y$.

Using this notation, the

$$\nabla_\sigma \cdot \overline{\overline{V_2 p_*}^{t}\overline{R}}^{t}$$

term in Eq. (3.7) can be expressed in approximate finite-difference form as

$$\nabla_\sigma \cdot \overline{\overline{V_2 p_*}^{t}\overline{R}}^{t} \approx \left(\sum_{\text{E}} - \sum_{\text{W}}\right)\left[\tfrac{1}{2}(u_0 p_{*0} + u_l p_{*l})\cdot\tfrac{1}{2}(R_0 + R_l)\cdot w_l\right] + \left(\sum_{\text{N}} - \sum_{\text{S}}\right)\left[\tfrac{1}{2}(v_0 p_{*0} + v_l p_{*l})\cdot\tfrac{1}{2}(R_0 + R_l)\cdot w_l\right], \tag{3.9}$$

where $\sum$ denotes a summation across all "0" and "l" box interfaces common to the side of the box indicated (E, W, N or S).

Here, the time averaging operator $\overline{(\,)}^{t}$ has been dropped for convenience. In the actual integration, the horizontal velocities u and v are time interpolations between successive 6 h time averages. Note that the interface interpolation for R is given by $\frac{1}{2}(R_0 + R_l)$, thus limiting the horizontal differencing to a maximum of second-order accuracy.

In the vertical, the grid arrangement is as given in Fig. 3 of Kurihara and Holloway (1967). The center of the key box is defined as being at level "K," while the boxes above and below the key box are designated as $K-1$ and $K+1$, respectively. The variables R, u, v and T are specified at the integer K levels, while $\dot{\sigma}$ is specified at the box interfaces $K-\frac{1}{2}$, $K+\frac{1}{2}$, etc.

The finite-difference form for the

$$\frac{\partial}{\partial\sigma}\overline{\dot{\sigma}\overline{p_*}^{t}\overline{R}}^{t}$$

term in Eq. (7) is

$$\frac{\partial}{\partial\sigma}\overline{\dot{\sigma}\overline{p_*}^{t}\overline{R}}^{t} \approx \frac{1}{(\sigma_{K+\frac{1}{2}} - \sigma_{K-\frac{1}{2}})} \times (\dot{\sigma} p_{*K+\frac{1}{2}} R_{K+\frac{1}{2}} - \dot{\sigma} p_{*K-\frac{1}{2}} R_{K-\frac{1}{2}}). \tag{3.10}$$

Thus, R at the "interface" levels must be determined by interpolation from the values of R at the "integer" levels. A second-order interpolation scheme which conserves the global integral of R and R^2 in the irregular grid is

$$R_{K+\frac{1}{2}} \approx \tfrac{1}{2}(R_{K+1} + R_K) \tag{3.11}$$

(Bryan, 1966; Kurihara and Holloway, 1967).

In this tracer problem, however, there are many circumstances in which R varies by orders of magnitude in the vertical. In such circumstances, the interpolation scheme of Eq. (3.11) can at times produce a significant overestimate of the value for $R_{K+\frac{1}{2}}$. This has the effect of overestimating the local flux whether it is up or down the local gradient. However, the overestimated upgradient flux often leads to prediction of negative values of R. These negative values of R are corrected in a mass conserving way (see Section 3b3), thus essentially reducing the upgradient fluxes. The overall effect then is to overestimate the magnitude of the net flux in the downgradient direction. Thus, a tracer released into the lower stratosphere can tend to be removed to the troposphere quite rapidly due as much to truncation error as to simulated transport.

One way to reduce the effect of such an error on the model calculation is to use a more accurate interpolation formula to determine the value of $R_{K+\frac{1}{2}}$. The method chosen for this model calculation is

$$R_{K+\frac{1}{2}} = \alpha(R_{K+1} + R_K) - \beta(R_{K+2} + R_{K-1}), \tag{3.12}$$

where $\alpha = \frac{9}{16}$ and $\beta = \frac{1}{16}$. These values of α and β correspond to Bessel's midpoint interpolation formula, which gives an exact value for $R_{K+\frac{1}{2}}$ if the vertical distribution of R can be represented by a fourth-order polynomial. Thus, the flux divergence of Eq. (3.10) can be regarded as being of fourth-order accuracy. This approach was thought to be more compatible with the essence of the box method than the usual fourth-order calculation of derivatives, which for Eq. (3.12) utilizes the coefficients $\alpha = 7/12$ and $\beta = 1/12$. Later work (Mahlman and Sinclair, 1977) suggests that this latter choice would probably have yielded a somewhat improved model performance.

At the half-levels next to the upper and lower boundaries (where $\dot{\sigma}=0$), the interpolated value of R is obtained by computing a noncentered value for the second derivative as it appears in Bessel's interpolation formula.

The above scheme for calculating

$$\frac{\partial}{\partial\sigma}\overline{\dot{\sigma}p_*}^{t}\overline{R}^{t}$$

in Eq. (3.7) has been found in preliminary experiments to suppress significantly the artificially large downgradient transport resulting from the use of the interpolation scheme of Eq. (3.11). It also conserves the global integral of R exactly

$$\left((\partial/\partial t)\int_G RdAp_*(d\sigma/g)=0\right).$$

However, the use of the fourth-order interpolation operation of Eq. (3.12) does not formally guarantee conservation of quadratic properties

$$\left((\partial/\partial t)\int_G R^2dAp_*(d\sigma/g)=0\right).$$

Fortunately, test computations have shown that the mixed-differencing accuracy leads to only a very mild damping of

$$\int_G R^2dAp_*(d\sigma/g)$$

with time. The magnitude of this damping is about the same as the damping of R^2 due to the occasional Euler backward time step to prevent solution separation and is within the magnitude of the small fluctuation of

$$\int_G R^2dAp_*(d\sigma/g)$$

due to time truncation error (see Section 3c). This damping is far less than that produced by the effects of DIFFUSION and FILLING.

3) Description of the negative mixing ratio adjustment scheme (FILLING)

As implied above, there are situations where truncation error in the calculation of the three-dimensional flux convergence leads to local prediction of negative mixing ratios. Since these negative values are not physically realizable, it is normally better to devise a scheme in which these negative values are "corrected" in a physically consistent manner such that all values in the field are either zero or positive. This computational correction appears as the FILLING term in Eq. (3.7).

A negative mixing ratio tends to be produced computationally when the advection is acting to replace comparatively large tracer values with much lower values. It normally occurs due to an overestimate of the flux out of the region resulting from interpolations between radically varying quantities. In this model such negative values are never allowed to remain, but are reset to zero with an accompanying subtraction of the required tracer mass from the appropriate neighboring grid box.

The appropriate neighbor box is selected by a method of "downstream borrowing." The largest of the flux divergence components acting to remove tracer is initially selected. Then the adjacent grid box in the appropriate downstream direction is selected for removal of enough tracer to reset the negative value to zero. In the event that the box selected does not contain an adequate amount of tracer to keep both tracer amounts positive, a search of the neighboring points to the selected box is employed.

These corrections are always done so that the mass integral of the tracer is exactly conserved (to the roundoff error of the computer). On the other hand, the effect of FILLING does produce a damping effect on the mass integral of the mean square of the tracer mixing ratio

$$\left((\partial/\partial t)\int_G R^2dAp_*(d\sigma/g)<0\right).$$

This occurs, of course, because the "borrowing" of tracer leads to a reduction of the absolute value of tracer in both participating grid boxes. This can be interpreted as a type of diffusive effect which is introduced into the model. In this experiment, special care is taken to insure that FILLING damping is dominated by DIFFUSION damping. This approach is taken because DIFFUSION represents an attempt to model a physically meaningful process, while FILLING is essentially a corrective response to a non-physical occurrence in the model.

4) Description of the subgrid-scale horizontal diffusion scheme (DIFFUSION)

One of the most difficult of the unsolved problems dealing with numerical simulations of geophysical fluid flows is to simulate properly the effects of transfers involving scales below the chosen grid resolution. Ideally, the magnitude and direction of this subgrid-scale transfer should be obtainable from the explicitly resolved variables. This type of parameterization cannot determine the exact nature of the subgrid-scale transfers, but should be designed to simulate such behavior in a statistically valid way.

In the absence of sources and sinks, the transfer of tracer through advection [as expressed in Eq. (3.6)] has the property of explicitly conserving the global

mass integral of the mean square of the tracer mixing ratio. However, for conservative tracers in the actual atmosphere, this integral is observed to be a decreasing function of time. Ultimately, of course, such an effect must be produced by molecular diffusion. This, however, is only important on scales far below those resolved in conventional meteorological grids.

In the problem addressed here, it is convenient to view the transport as being dominated by advection in the resolved scales. However, the advection process is visualized as systematically converting large-scale gradients of tracer into smaller scale gradients through the simulated processes of fluid deformation. (It should be noted that this process itself is somewhat inhibited because the simulated air motions themselves only contain scales as large as those allowed by the basic grid.) This process of deforming to smaller scales may thus be thought of as setting the stage for processes which are ultimately diffusive in character.

From this point of view, a desirable scheme for parameterizing the subgrid-scale transfers is one in which the larger resolved scales of variability are virtually unaffected, but one which acts to prevent a buildup of scales of variability near that of the grid scale itself. At present, there exists no fully satisfactory theoretical or empirical basis for accomplishing this. Further, a scheme which is acceptable at a given resolution may not be acceptable at another resolution. At very coarse resolutions, the essential processes are often no longer resolved by the grid. One approach is to work with a high enough resolution that the simulated behavior at the scales of interest is nearly independent of the method of parameterization of the subgrid-scale transport. In practice, however, this is usually very difficult because of the excessive computational requirements for such high-resolution systems. Generally, any parameterization of the subgrid-scale transports should be compatible with the individual character of the problem under consideration and with the numerical approximations chosen for that problem.

Historically, it has been convenient to assume that the subgrid-scale transfer can be given by a macroscale analog to molecular diffusion, where the coefficient of "eddy diffusivity" is an empirically determined constant expressing the statistical transfer rate totally in terms of the large-scale gradient of the transferred quantity. Such an approach may or may not have any real relationship to the actual transfer process. The experiment described here has been run for periods of one month using various constant eddy diffusion coefficients. The results show that such a formulation of the subgrid-scale transfers leads to an undesirably large amount of damping of the larger scales when the eddy coefficient is large enough to prevent a buildup of variability in the scales near the grid resolution. In short, this technique is insufficiently scale selective, and as a result, tends to suppress the effect of the advective transport by the explicitly resolved motions. Since the motivation for this study is largely to test the effect of the large-scale motions on transport, such an approach is undesirable.

A more meaningful approach is to employ a formulation in the spirit of that introduced by Smagorinsky (1963), in which the form of the subgrid-scale transfer is assumed to be specifiable in terms of the local explicitly determined variables. This method is based upon the assumption that the subgrid-scale energy transfer is dominated by the isotropic inertial subrange (no local production or dissipation, only inertial transfer to progressively smaller scales). Although there is no obvious physical reason for this assumption to be valid for the large-scale transfers of interest here, the Smagorinsky approach has provided useful results in a variety of applications, including the GCM used for this tracer study.

By applying dimensional arguments consonant with the Smagorinsky formulation to the problem of transfer of a passive tracer, one obtains for the "eddy diffusivity"

$$K_H = C l_s^2 |D| \rho^2, \tag{3.13}$$

where C is an unspecified dimensionless constant, l_s a length scale characteristic of the subgrid-scale transport processes, $|D|$ the magnitude of the model-resolved horizontal velocity deformation, and ρ the interface linear correlation coefficient between the subgrid-scale tracer and the velocity component normal to the interface, or alternatively, the subgrid-scale transport "efficiency." Normally, ρ is implicitly assumed to be a constant which is independent of local conditions.

Although ρ is not really a constant, it is unclear just what form it should take. Intuitively, the following form seems reasonable:

$$|\rho|_{0,l} = Q + (1-Q)\left|\frac{R_0 - R_l}{R_0 + R_l}\right|, \tag{3.14}$$

where Q is a constant which can range from 0 to 1. If $Q=1.0$, then Eq. (3.14) gives $\rho=1.0$, thus reverting to the previous assumption about ρ. On the other hand, if $Q=0$, then $\rho_{0,l}$ is assumed to be determined completely by the relative variability of the tracer field across the box interface. A functional dependence of this type appears reasonable because the probability of a high tracer-normal velocity correlation should increase in some fashion as the relative variability increases across the interface. This is because at high relative variability (where one box is nearly depleted relative to the other), virtually any combination of subgrid-scale motions will lead to large values of ρ. On the other hand, at low relative variability, the subgrid-scale variations within a box become of the same magnitude as the variations across the box. In this circumstance, a low tracer-normal velocity correlation is expected at the interface.

For the present experiment, the values chosen are

TABLE 2. Examples of the effect of various (normalized) tracer distributions on the eddy diffusivity $K_{H_{0,l}}$ of Eq. (3.16)

R_0	R_l	$\frac{R_0-R_l}{R_0+R_l}$	$\left(\frac{R_0-R_l}{R_0+R_l}\right)^2$
1.00	0.90	0.0526	0.0028
1.00	0.80	0.1111	0.0123
1.00	0.70	0.1765	0.0311
1.00	0.50	0.3333	0.1111
1.00	0.30	0.5385	0.2899
1.00	0.10	0.8182	0.6694
1.00	0.05	0.9048	0.8186
1.00	0.00	1.0000	1.0000

$C=10$ and $Q=0$. This choice gives maximum weighting to the local tracer variability in assessing the value of K_H.[1] In addition, the value of l_s in Eq. (3.13) for this study and for the "parent" GCM is assumed to be

$$l_s=0.2\Delta S, \tag{3.15}$$

where ΔS is the average grid size. This form for l_s is compatible with the theoretical predictions of Deardorff (1971), as well as with the empirical determinations of Miyakoda *et al.* (1971).

Introducing these assumptions into Eq. (3.14) gives

$$K_{H_{0,l}}=10(0.2\Delta S)^2|D|_{0,l}\left(\frac{R_0-R_l}{R_0+R_l}\right)^2. \tag{3.16}$$

The inclusion of the tracer variability dependence in Eq. (3.16) acts to increase markedly the scale selectivity of the modeled subgrid-scale tracer transfer. This effect is demonstrated in Table 2.

In the usual K_H formulation (and as applied in the GCM for this experiment), it is assumed that $C=1$ and $\rho=1$ in Eq. (3.13). Table 2 thus shows that the formulation of Eq. (3.16) yields values of K_H larger than the usual formulation only when there is more than about a factor of 2 variation in R across the interface. For lesser variability, the values of K_H are much smaller than in the usual formulation.

For the problem under investigation here, the subgrid-scale transfer is parameterized in terms of the explicitly resolved variables by setting

$$\text{DIFFUSION}=\nabla_\sigma\cdot p_*K_H\nabla_z R, \tag{3.17}$$

where ∇_z is the horizontal gradient operator. Thus, the form of DIFFUSION in Eq. (3.17) is not a strict transformation of a height-coordinate version, but rather a flux divergence in the σ coordinate with the interface fluxes representing subgrid-scale horizontal transports in response to horizontal gradients.

By writing Eq. (3.17) in component form and transforming $\nabla_z R$ to σ coordinates, one obtains

$$\text{DIFFUSION}=\frac{\partial}{a\cos\phi\partial\lambda_\sigma}\left[K_H\left(p_*\frac{\partial R}{a\cos\phi\partial\lambda_\sigma}-\sigma\frac{\partial R}{\partial\sigma}\frac{\partial p_*}{a\cos\phi\partial\lambda_\sigma}\right)\right]+\frac{1}{\cos\phi}\frac{\partial}{a\partial\phi_\sigma}\times\left[K_H\cos\phi\left(\frac{p_*}{a}\frac{\partial R}{\partial\phi_\sigma}-\sigma\frac{\partial R}{\partial\sigma}\frac{\partial p_*}{a\partial\phi_\sigma}\right)\right]. \tag{3.18}$$

Again, by applying the box method of Kurihara and Holloway (1967) in analogous fashion to Eq. (3.9), one can write Eq. (3.18) in the approximate form

$$\text{DIFFUSION}\approx\left(\sum_{\text{E}}+\sum_{\text{W}}+\sum_{\text{N}}+\sum_{\text{S}}\right)\times\left\{w_lK_{H_{0,l}}\left[\tfrac{1}{2}(p_{*0}+p_{*l})(R_l-R_0)\overline{w_{0,l}}-\sigma\left[\frac{\tfrac{1}{2}(R_{l,K+1}+R_{0,K+1})-\tfrac{1}{2}(R_{l,K-1}+R_{0,K-1})}{\sigma_{K+1}-\sigma_{K-1}}\right]\times(p_{*l}-p_{*0})\overline{w_{0,l}}\right]\right\}, \tag{3.19}$$

where all variables are calculated at level K unless specifically noted. In Eq. (3.19), $\overline{w_{0,l}}$ is the average of the weight (w_l) for the $0,l$ interface for the "0" box and the weight for the same $0,l$ interface but for the "l" box. This procedure insures conservation of tracer mass by guaranteeing that the flux is identical on each side of the interface. Since the common interface length is the same in each case, $\overline{w_{0,l}}$ is equal to w_l when $A_{\text{box}(0)}=A_{\text{box}(l)}$ (e.g., for boxes aligned in the zonal direction).

The local "eddy diffusion" coefficient $K_{H_{0,l}}$ [Eq. (3.16)] applicable to the $0,l$ interface is calculated by

East and west interfaces

$$K_{H_{0,l}}=C(k_0\Delta S)^2|v_0-v_l|w_l\left(\frac{R_0-R_l}{R_0+R_l}\right)^2 \tag{3.20a}$$

North and south interfaces

$$K_{H_{0,l}}=C(k_0\Delta S)^2|u_0-u_l|\overline{w_{0,l}}\left(\frac{R_0-R_l}{R_0+R_l}\right)^2. \tag{3.20b}$$

The horizontal velocity deformation $|D|$ is very crudely approximated in Eqs. (3.20a) and (3.20b) by using only the magnitude of the normal derivative of the velocity component parallel to the given interface. This extreme simplification of deformation was chosen because of the crudeness of the diffusion theory, the severity of the computational burden required to

[1] Later experiments with less variable tracers suggest that values of $Q\approx0.15$–0.25 give optimal results.

calculate DIFFUSION, and the particular computer input/output requirements for the irregular grid.

5) Discussion of vertical subgrid-scale diffusion

The experiment presented here is intended to provide a test of the ability of the explicitly resolved motions in the GCM to provide an accurate transport of trace substances. The horizontal subgrid-scale parameterization of the previous section was formulated with this goal in mind.

At present, there remains some controversy as to how important the small-scale motions in the stratosphere are for effecting a systematic vertical tracer transport. Because of this, the point source tracer problem described in this paper was executed for a one-month period using two separate values of constant vertical eddy diffusion coefficients, 0.5 $m^2\ s^{-1}$ and 0.1 $m^2\ s^{-1}$. In both cases, the tracer transport from the stratosphere to the troposphere was drastically overestimated compared with observed behavior of radioactive tracers. However, an eddy diffusivity of 0.1 $m^2\ s^{-1}$ is at the lower end of the range commonly assumed to describe total vertical transfer in the stratosphere. The above result suggests that subgrid-scale motions are considerably less important than large-scale motions in effecting stratospheric vertical tracer transfer. This inference is strengthened by analyses of Project HICAT spectra (e.g., Lilly *et al.*, 1974).

For this experiment, the vertical eddy diffusivity has been set to zero. This is not to say that vertical subgrid-scale transports are totally unimportant, but only that they are assumed to be small relative to the large-scale transports. This experiment thus examines the hypothesis that large-scale motions are the dominant component in vertical tracer transfer in the lower stratosphere. The assumption of zero vertical eddy diffusion, although probably reasonable for the stratosphere, should lead to an underestimate of the vertical transfer rate in the troposphere, especially near the earth's surface. However, because the time scales for vertical transfer in the model troposphere are much faster than for the model stratosphere, the net removal rate from the stratosphere is rather insensitive to this omission.

6) Description of parameterization of sources and sinks

In the experiment described here, the only SOURCE effect introduced is at the start of the experiment. For simplicity, it is described in Section 4, which discusses the design of the experiment of this paper.

The only SINK modeled simulates the local removal of tracer within the troposphere. Its specific form for inclusion in Eq. (3.7) is given by

$$\text{SINKS}=p_*(C_{\text{dry}}+C_{\text{wet}})R, \tag{3.21}$$

where C_{dry} and C_{wet} are empirical coefficients representing dry and rainfall-dependent tracer removal processes, respectively. C_{dry} is activated only at the bottom two levels, representing removal processes in the boundary layer. Expressed as an effective removal time in the effect of the SINKS in Eq. (3.7), the values used in this experiment are $C_{\text{dry}}^{-1}(\sigma=0.990)=20$ days and $C_{\text{dry}}^{-1}(\sigma=0.940)=30$ days. These choices are based on removal rates estimated from the behavior of radioactive particulates in dry surface air.

The rainfall-dependent removal coefficients are assumed to be negligibly small above $\sigma=0.315$ and a function of the precipitation rate below. The wet removal coefficient is scaled so that

$$C_{\text{wet}}=B(\text{RAIN}/\overline{\text{RAIN}}^{G}), \tag{3.22}$$

where RAIN is the total precipitation calculated at the given grid point over a 6 h period, while $\overline{\text{RAIN}}^{G}$ is the global average precipitation rate expressed as deposition per 6 h. B is interpreted as the effective removal coefficient if it is precipitating locally at the global average rate. The value of B is scaled so as to remove tracer from the bottom subcloud levels at approximately the dry rate for the case when $\text{RAIN}=\overline{\text{RAIN}}^{G}$. Above the boundary layer, the removal efficiency is assumed to decrease with altitude in a way roughly consistent with average observed contributions of each layer to the total precipitation rate. The reciprocal values of B utilized in these experiments are

$B^{-1}(\sigma=0.990)=20$ days; $B^{-1}(\sigma=0.940)=25$ days;
$B^{-1}(\sigma=0.835)=30$ days; $B^{-1}(\sigma=0.685)=40$ days;
$B^{-1}(\sigma=0.500)=50$ days; $B^{-1}(\sigma=0.315)=60$ days.

In preliminary experiments, the net removal of tracer was essentially insensitive to variations of a factor of 2 in the removal coefficients. This appears to result mainly because, at typical precipitation rates, a large portion of the local tracer is removed over the precipitation event for virtually any values of B in the magnitude range of those used here. With this scheme, the total wet removal is significantly larger than the total dry removal. This is because the wet removal is operative above the boundary layer in a region where the R values are larger and the layers more massive than at the ground. For the present experiment, about 85% of the total tracer removal is due to moist processes.

7) Discussion of particulate settling in the stratosphere

It has been known for some time that much of the radioactive debris in the stratosphere is attached to submicron size particles. This effect was reviewed in some detail by Telegadas and List (1969) who concluded that gravitational settling of particulate radioactivity

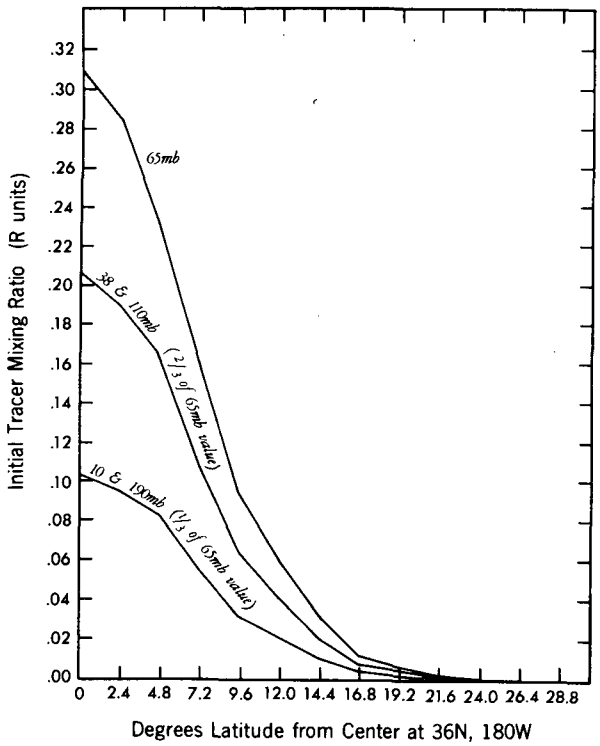

FIG. 4.1. Initial tracer distribution (R units) of experiment in terms of distance from the center at 36°N, 180°W.

is probably a significant effect only on time scales longer than a year after detonation. This inference has been disputed by Johnston *et al.* (1976), who suggest that radioactive particles could ionize the surrounding air and act as condensation nuclei for aqueous sulfuric acid, thus acting to increase the typical particle size and increase the settling speed so that it is effective immediately after detonation.

Because the Stokes settling speed is strongly dependent upon particle size (Junge *et al.*, 1961), it is very difficult to develop an acceptable scheme for including particulate settling in a model. In addition, the physics of particle formation and coagulation is poorly understood. Consequently, for this experiment, a settling effect has not been included. As will be shown in Section 5a4, the omission of settling leads to some interesting interpretations of this experiment in terms of the probable differences between the behavior of gaseous and particulate tracers.

c. *Method of time integration*

For the time integration of Eq. (3.7), centered leapfrog extrapolation is used for the advective terms. For the DIFFUSION and SINK terms, a simple forward Euler step is employed. To prevent the weak time splitting instability associated with the leapfrog method, an Euler-backward step is included once per model day. To insure computational stability everywhere in the domain, a time step of 24 min is used.

Due to the prohibitive computational cost of integrating a high-resolution GCM, only one year of wind data is available. The tracer integrations proceed longer than a year by "recycling" the same input wind data each year. A disadvantage of this procedure is that there is no interannual variability in the controlling meteorology. However, at the present stage of the research, this turns out to be an advantage for interpretative purposes. This is particularly so in Section 5b which shows interesting year-to-year variations in various tracer balances due to evolving tracer distributions.

Another disadvantage of the input wind "recycling" (done on 1 August each model year) is that it produces a discontinuity in the wind field across that date. In turn, a mild shock appears in the tracer field until it adjusts locally in several days to the somewhat different wind field.

4. Description of the experiment

a. *Observational counterparts*

A number of thermonuclear weapons tests have been conducted in midlatitudes of the Northern Hemisphere, some of which were followed by significant measurements of the subsequent debris distributions in the stratosphere. Systematic analysis of these measurements has been reported by Machta and Telegadas (1973) and others. Their results indicate that the long-term (>6 months) evolution of such debris is essentially independent of the specific meteorological conditions and time of year of the midlatitude, lower stratosphere injections.

Such a result suggests that the long-term behavior of a numerical experiment attempting to simulate such a release is probably not too sensitive to the particular details of the initial conditions. This is an important consideration for the kind of experiment performed here, because the GCM does not attempt to consistently produce an exact duplicate of a given sequence of meteorological events. Rather, it generates its own sequence of motions which, if successful, should exhibit statistical behavior which strongly resembles that of the actual atmosphere.

b. *The initial condition*

The SOURCE term for this experiment is set as an initial condition at the beginning of the integration. It is designed to simulate a diffuse source of tracer in the stratosphere, somewhat analogous to a megaton range nuclear detonation.

The initial tracer field is set on 1 January with its center at 36°N, 180°E. This initial distribution is spread over a significant volume to reduce the large space-truncation error that occurs when the relative mixing ratio gradients are large. The center of the initial

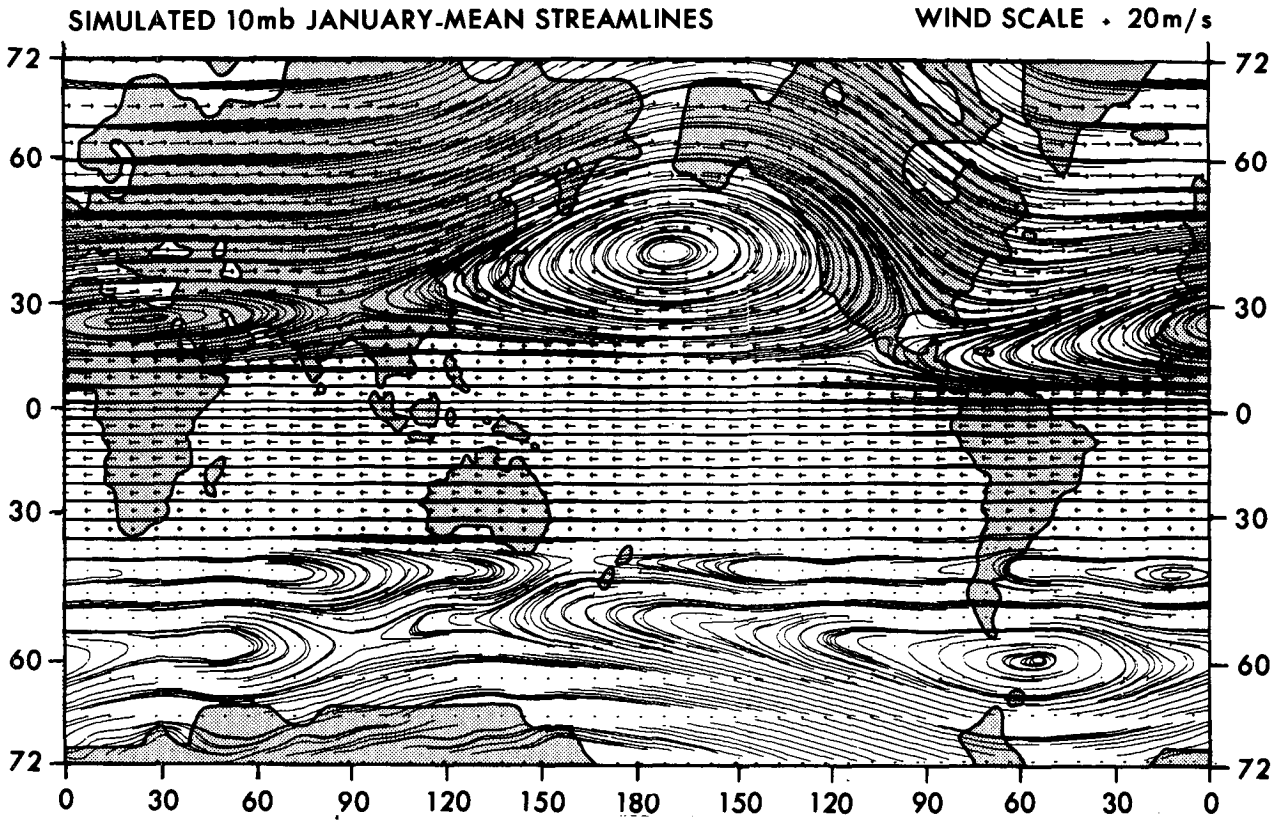

FIG. 4.2. Mercator projection of GCM January mean streamlines at 10 mb level. Arrows show local wind vectors with length proportional to speed as indicated at upper right.

tracer is at 65 mb, with mixing ratios $\frac{2}{3}$ and $\frac{1}{3}$ of the 65 mb value at the first and second adjacent vertical levels, respectively. The horizontal distribution decays away from the center symmetrically. Fig. 4.1 gives the distribution for the various model levels.[2] This initial distribution is such that 65% of the tracer mass is located within 10° latitude of the source center, 90% within 15° latitude, and 98% within 20° latitude. Such a distribution insures that most of the initial tracer is contained within a single stratospheric disturbance, while drastically reducing the transport and damping due to FILLING that would occur in the initial stages if the source were more compactly distributed.

Figs. 4.2 and 4.3 show model-produced vector streamline charts for the January mean flow at 10 and 190 mb. The mean flow patterns seen in these figures may be contrasted with the instantaneous 1 January fields at 10 and 65 mb given by Mahlman (1973b). These figures show the very pronounced presence of the simulated Aleutian anticyclone and Japan jet systems, respectively (for more detailed discussion, see MM76), and also indicate that the center of the initial injection is in the anticyclonic region.

At first glance, this may appear to be a surprising choice for placement of the initial tracer because no thermonuclear weapons tests have ever been conducted at that location. However, this does not appear to be an important consideration in view of the previously mentioned observations that long-term tracer evolutions are insensitive to details of the initial condition. This particular choice was selected for another reason. It has been observed that ozone and radioactivity in the lower stratosphere are highly correlated with potential vorticity in the zonal mean (Hering, 1965) and locally (Danielsen, 1968; Danielsen *et al.*, 1970). This initial condition is thus set to establish a very low beginning correlation of the tracer mixing ratio with the potential vorticity field. Some aspects of the evolution of this correlation in the model will be described in Section 5a3.

5. Experimental results

a. Large-scale behavior

1) EVOLUTION OF THE ZONAL MEAN

A simple way to gain a rather comprehensive view of the behavior of this experiment is to examine the zonal

[2] Because the tracer mixing ratio in this experiment is expressed in arbitrary dimensionless units, it is convenient for discussion purposes to give this unit a name. Because *R* is its symbol, the "*R* unit" is designated for purposes of convenience. This unit can be readily converted to a specific unit when applied to a particular problem.

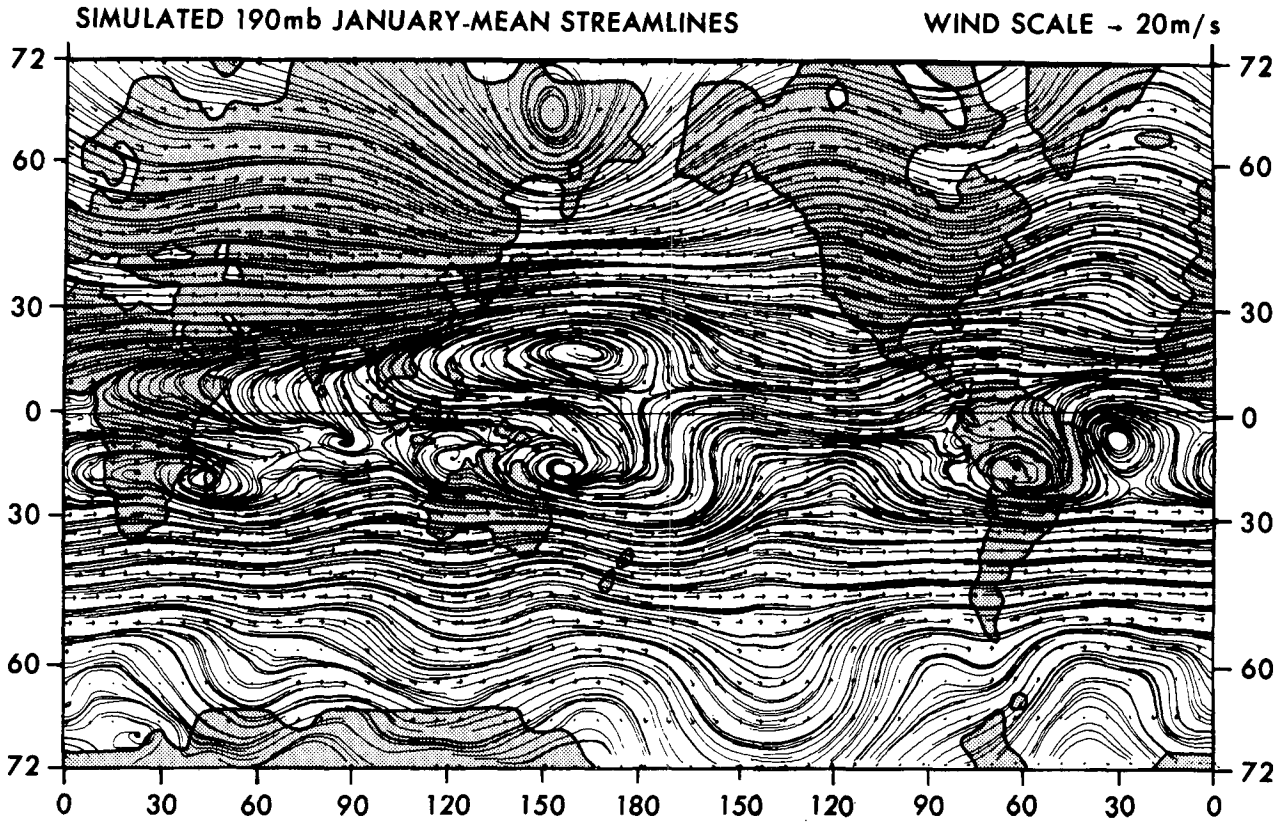

FIG. 4.3. As in Fig. 4.2 except for 190 mb.

mean structure of the tracer field as it evolves in time. Fig. 5.1 shows the distribution of $\overline{\overline{R}^{\lambda}}^{t}$ [where $\overline{(\ )}^{\lambda}$ is a zonal average and $\overline{(\ )}^{t}$ a time average] for the months of January, April, July and October for the four years of this experiment.

In April of year 1, there is considerable evidence of rapid dispersion away from the region of the initial release. Most notable are the large protrusions downward into the troposphere near 30°N and into the Southern Hemisphere in the lower stratosphere. Discussions on the mechanisms responsible for the various features seen in Fig. 5.1 will appear in later sections. By July of year 1, it is evident that a strong poleward-downward movement of tracer has occurred. This is particularly clear in the Northern Hemisphere high latitudes associated with the simulated spring reversal of winds from westerlies to easterlies (see MM76). The strong push of tracer into the Southern Hemisphere is most evident just above the tropopause. In fact, it has led to tracer minima in the South Pole region near the ground and in the middle stratosphere. The October year 1 cross section shows continued dispersion, but the most prominent feature is a strong downward protrusion at about 20–45°S, and extending from 38 mb down into the troposphere. The second year (Fig. 5.1b) is marked by a pronounced slowing down of the apparent dispersion rate. Also, the highest mixing ratios are approaching the top model level.

By the third year (Fig. 5.1c) the global-scale dispersion is evolving slowly enough that seasonal effects are beginning to dominate. After the Northern Hemisphere spring reversal in the zonal wind, the zonal mean mixing ratio is increasing upward everywhere in the model stratosphere. Also, Fig. 5.1c indicates that a distinct minimum in $\overline{\overline{R}^{\lambda}}^{t}$ appears in the equatorial stratosphere.

During year 4, Fig. 5.1d shows that the equatorial minimum has extended to the top of the model atmosphere so that smaller equatorial values separate higher mixing ratios in the middle-latitude stratosphere of each hemisphere. The difference in mixing ratios between the hemispheres is now relatively small compared to the first two years of the experiment. However, the seasonal effects mentioned above remain strongly evident.

Because of the large magnitude ranges of tracer present during this experiment, it has been necessary to choose logarithmic contour intervals for the cross sections of Fig. 5.1 and others. Unfortunately, this can easily lead to the perception that the model tropopause is rather poorly defined in terms of the vertical tracer structure. This can be shown to be a misleading perception by viewing vertical profiles of $\overline{\overline{R}^{\lambda}}^{t}$ plotted with

a linear abscissa. Examples are given in Fig. 5.2 which illustrate significant changes in the vertical gradient of $\overline{R}^{t}_{\overline{\lambda}}$ above the simulated zonal-mean tropopause at 0°N (110 mb), 30°N (190 mb) and 60°N (315 mb). Note also that this tropopause effect is not as apparent in the global average vertical profile of R shown in Fig. 5.2.

2) Comparison of the zonal mean with observations

Since this model has not been explicitly "tuned" to agree with trace constituent observations, a comparison of these results with the behavior of real tracers is of special significance. Possibly the closest analog to this experiment is the Chinese high-yield (3 megaton) nuclear test of 7 December 1968. It was an air burst at about 40°N which injected most of its debris between 15 and 20 km (Machta and Telegadas, 1973). This center of injection is thus quite consistent with the largest values in the model experiment initial condition shown in Fig. 5.1a. However, a significant difference is apparent in the amount of initial tracer that this experiment introduces above 20 km for reasons of computational consistency.

An additional source of complication in comparing this experiment to the behavior of nuclear weapons debris is the possible effect of particulate settling. As explained in Sections 3b6 and 3b7, this experiment should be visualized as being more analogous to a water-soluble gaseous tracer. It thus may yield long-term behavior quite different from that of radioactive substances which become attached to particles in the stratosphere.

The distribution of particulate Zr^{95} (decay corrected) for the 14–29 July 1969 period following the 28 December 1968 test is shown in Fig. 5.3. Comparison of Fig. 5.3 with the simulated July cross section of Fig. 5.1a reveals a number of interesting features. The similarities are the average poleward-downward slope of the mixing ratio contours, the strong relative stratification just above the tropopause, and the protrusion of tracer into the lower stratosphere of the Southern Hemisphere. Points of disagreement are that the experiment exhibits a higher altitude of the maximum mixing ratios, an apparently stronger transport into the Southern Hemisphere, and a less pronounced downward protrusion into the high-latitude lower stratosphere. It is not clear whether or not the latter difference is a model deficiency or related to a relatively poor sampling of the radioactivity in the 8–15 km region.

The period following the December 1962 moratorium in atmospheric testing of nuclear weapons also provides useful samples of tracer behavior to compare against this simulation experiment. Fig. 5.4 shows decay-corrected January–April zonal averages for 1963, 1964 and 1965 of Mn^{54}, a particulate radioactive tracer with a decay half-life of 312 days (Feely *et al.*, 1966). These data indicate qualitative features similar to those given in Fig. 5.3. In addition, the center of mass of the Mn^{54} raises somewhat as time progresses. However, this effect is not nearly as pronounced as seen in the model data illustrated in Fig. 5.1. The difference between observation and this experiment is probably attributable to the added effect of particulate settling present in the actual atmosphere, but which is not included in the model.

3) Relation of tracer mixing ratio to isentropic and potential vorticity surfaces

A number of authors have pointed out the apparent close relationship in the lower stratosphere between quasi-conservative trace constituents and the isentropic potential vorticity [$P=-(\partial\theta/\partial p)(f+\xi_{r\theta})$, where $\xi_{r\theta}$ is the vertical component of relative vorticity evaluated on an isentropic surface, θ the potential temperature and f the Coriolis parameter]. Most notably, Hering (1965) pointed out that bimonthly longitudinal means of ozone and radioactive tracers averaged over North America correlate well with P. Danielsen *et al.* (1970) demonstrated that this correlation extends into mesoscale features as well.

These studies suggest that similar relationships should hold in the numerical experiment described here. To examine this, Fig. 5.5 shows comparisons for January and July, year 4, between simulated tracer mixing ratio and potential vorticity of the zonal mean structure in the "parent" GCM. These results show a similar correspondence to that given by Hering (1965). As expected, the relationship breaks down near the equator where the potential vorticity approaches zero.

A closer examination of Fig. 5.5 indicates that, while the relationship is not exact, the correspondence is closer in the summer hemispheres. In the Northern Hemisphere during January, the midlatitude tracer slopes are somewhat steeper than those of the potential vorticity. Furthermore, the tracer maximum appears at a slightly higher latitude than the potential vorticity maximum. These differences appear to arise because the tracer mixing ratio is more conservative than the potential vorticity in this experiment.

The departures are not nearly so evident in the Southern Hemisphere during July. As pointed out in MM76, the stratospheric winter planetary wave activity in this model is much larger in the Northern Hemisphere than in the Southern Hemisphere. Such processes lead to much larger local magnitudes of eddy potential vorticity in the Northern Hemisphere. Recall, however, that potential vorticity is altered by vertical gradients of diabatic heating as well as by small-scale dissipative processes. Thus, it appears plausible to hypothesize that destruction of potential vorticity perturbations takes place more efficiently in the Northern Hemisphere winter stratosphere than in the Southern Hemisphere winter stratosphere. Such an enhanced potential

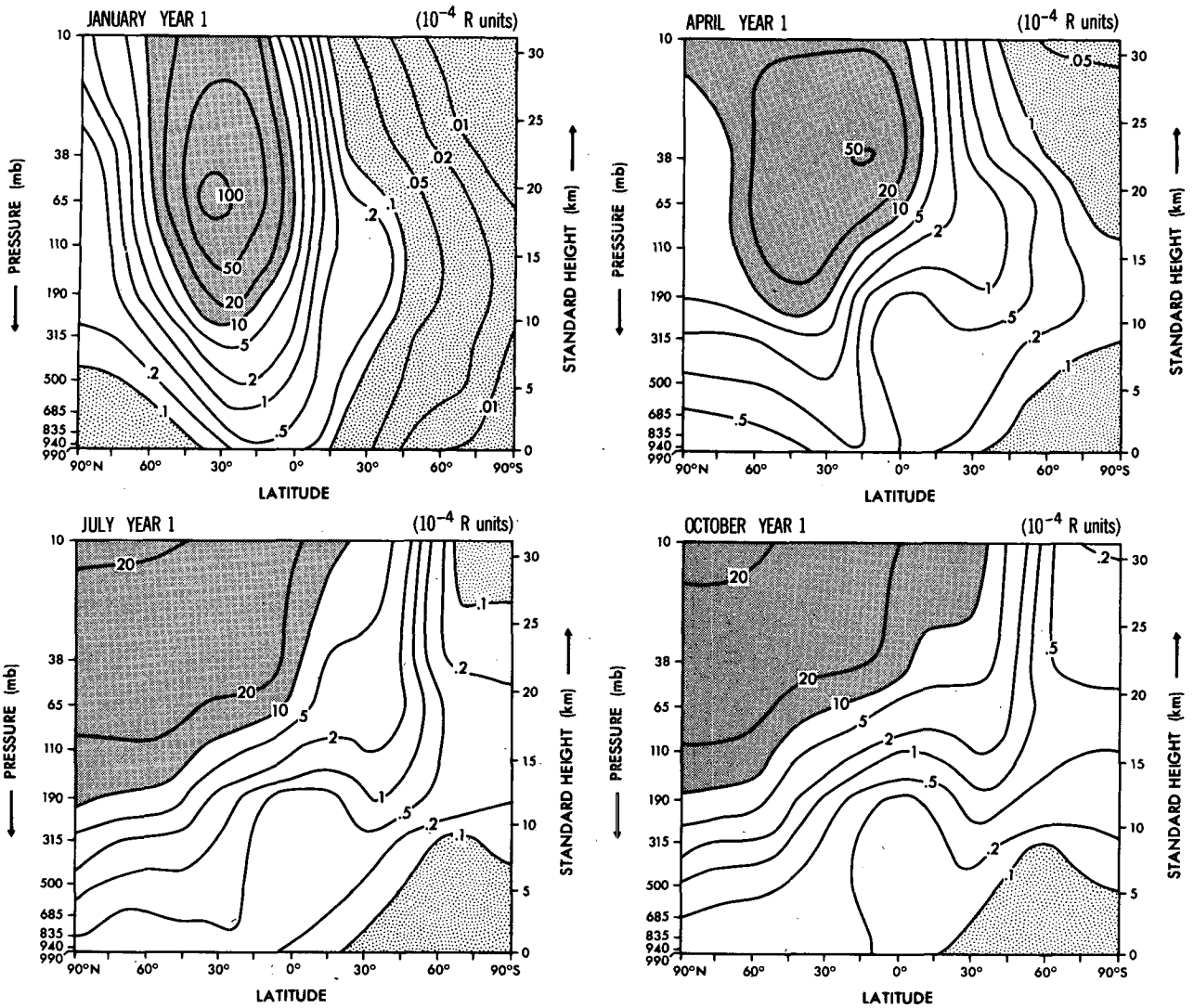

FIG. 5.1a. Zonal mean tracer mixing ratio (10^{-4} R units) averaged over indicated months for the firsrt year of the expeiment. Logarithmic contour intervals.

vorticity destruction could then lead to some decoupling of the usual tight correspondence expected between R and P. For an analysis of the stratospheric potential vorticity budgets, see Hartmann (1977).

Support for this argument can be gained by comparing the model zonal-mean potential temperature (θ) surfaces with those of tracer and potential vorticity. Such a comparison shows that the poleward-downward slopes are smaller than those of $\overline{R}^{\lambda}$ and $\overline{P}^{\lambda}$. In addition, the lower stratospheric $\overline{\theta}^{\lambda}$ maximum (midlatitude warm belt) is about 10° latitude equatorward of the maximum in $\overline{P}^{\lambda}$. The flatter $\overline{\theta}^{\lambda}$ surfaces are consistent with the observational studies of Newell (1961) and of Machta and Telegadas (1973). Also, both results are consistent with the expectation that potential temperature in the lower stratosphere is considerably less conservative than either potential vorticity, ozone or radioactive tracers.

Another interesting question concerns the degree with which the model tracer correlates locally with the model potential vorticity. As stated in Section 4b, the initial condition for this experiment was designed to establish a very small local tracer/potential vorticity correlation.

Fig. 5.6 shows a time series of the global correlation coefficient between R and P evaluated as a function of model level and at the first of each model month. The calculation reveals that the correlation grows to moderate values within one month, but that very high stratospheric correlations evolve on a time scale of about one-half year.

Over longer time scales, it is quite reasonable to expect a high local correlation to evolve between R

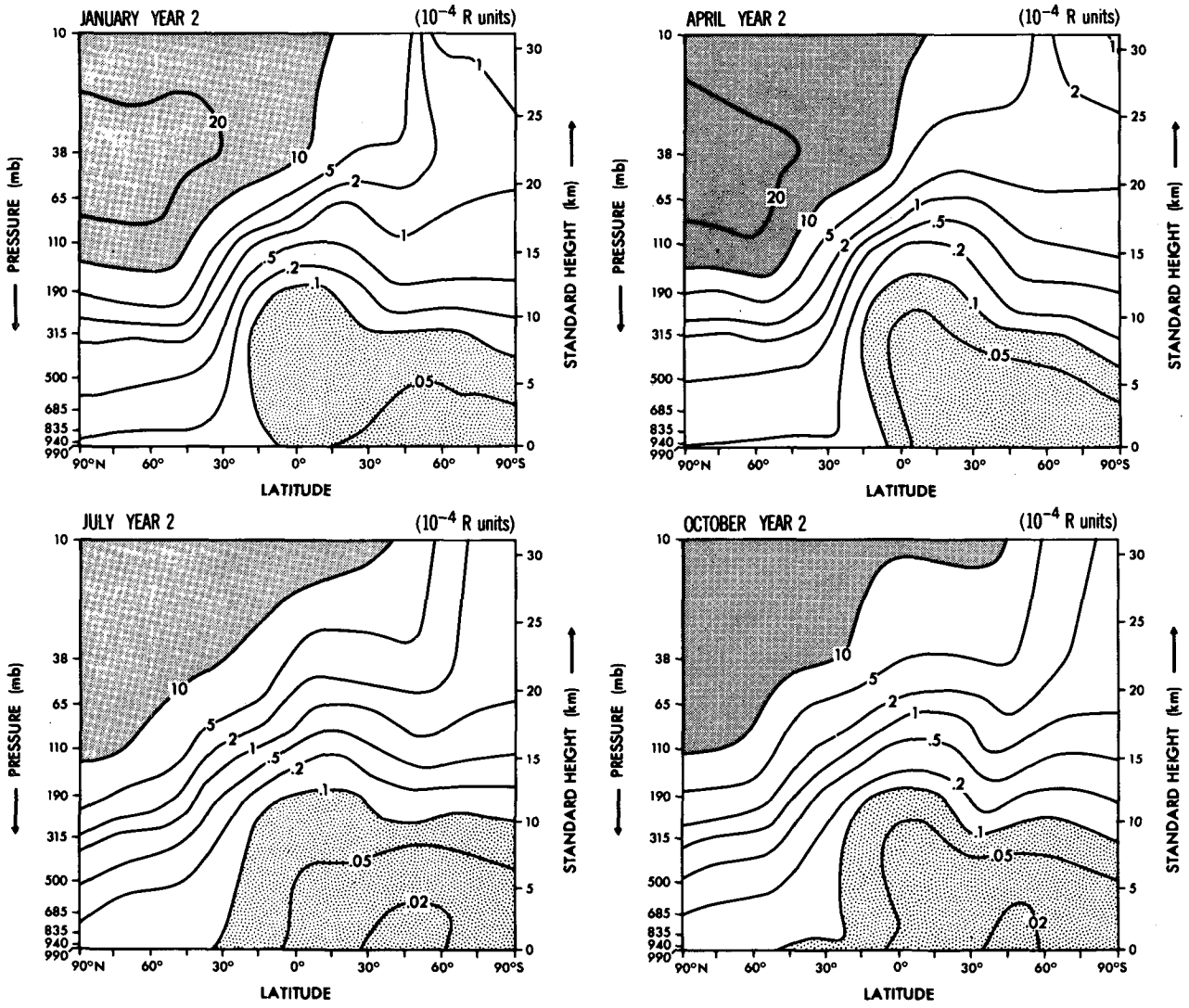

FIG. 5.1b. As in Fig. 5.1a except for year 2.

and P. This is because both R and P are quasi-conservative and become similarly stratified in the vertical, as is evident in Fig. 5.5. When that occurs, almost any combination of vertical motions will produce similar effects on R and P, thus leading to a high correlation.

Fig. 5.6 shows a rapid increase in the R, P correlation by the end of the first month. This correlation must first occur in the eddies, as the $\overline{R}^{\lambda}$ structure evolves more slowly. It is interesting to observe that this correlation evolves rapidly even at 10 and 38 mb, where Fig. 5.1 shows that R tends to decrease or remain nearly constant with increasing altitude. A plausible explanation for this can be found in the model energetics as calculated in MM76 (Figs. 9.1–9.4) which show the dependence of the stratospheric disturbances upon the troposphere. In mid and high northern latitudes, the model creation of eddy kinetic energy at 10 mb is due mainly to the sum of the two terms

$$\overline{-\omega'\alpha'}^{\lambda} - \overline{\frac{\partial}{\partial p}\omega'\Phi'}^{\lambda} = \overline{\Phi'\nabla_p\cdot\mathbf{V}'}^{\lambda} \approx 0.5\times10^{-2}\ \mathrm{W\ Kg^{-1}}, \quad (5.1)$$

where α is specific volume and Φ is geopotential. This result indicates systematic convergence into lows (small ϕ' and large P') and divergence out of highs (large ϕ' and smaller P'). It remains to determine the time scale over which this process is effective. From the definition of the linear correlation coefficient (ρ) one can evaluate

$$(\overline{(\nabla_p\cdot\mathbf{V}')^2}^{\lambda})^{\frac{1}{2}} = \frac{\overline{\phi'\nabla_p\cdot\mathbf{V}'}^{\lambda}}{\rho(\overline{\phi'^2}^{\lambda})^{\frac{1}{2}}}. \quad (5.2)$$

From the GCM for 10 mb January poleward of 40°N,

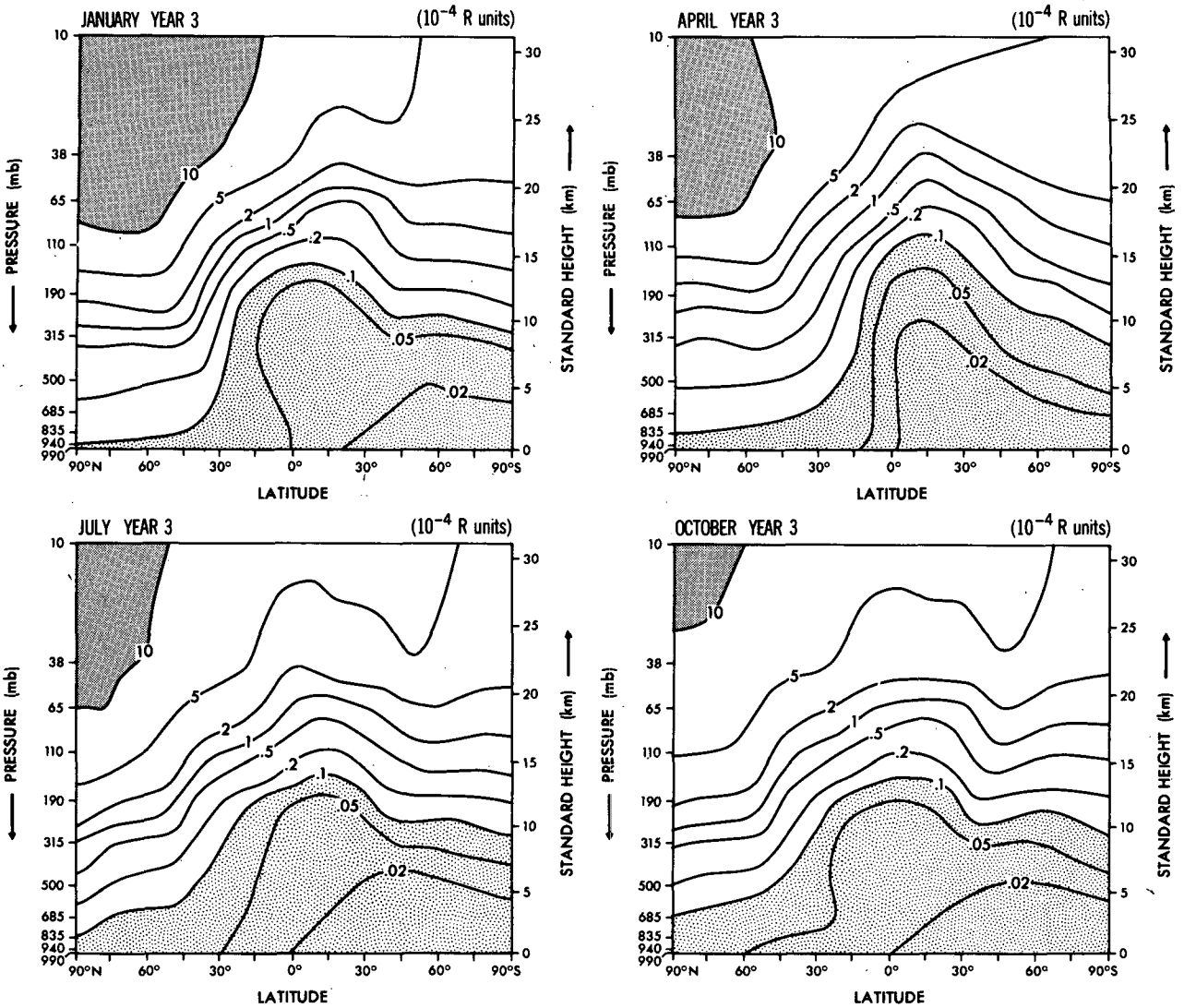

FIG. 5.1c. As in Fig. 5.1a except for year 3.

$\rho \approx +0.7$ and

$$(\overline{\phi'^2}^{\lambda})^{\frac{1}{2}} \approx 1 \times 10^4 \text{ m}^2 \text{ s}^{-2}.$$

This gives

$$(\overline{(\nabla_p \cdot \mathbf{V}')^2}^{\lambda})^{\frac{1}{2}} \approx 0.7 \times 10^{-6} \text{ s}^{-1}.$$

For a constant divergence field this can be interpreted as a reciprocal time scale which, from the values appropriate for Eq. (5.2), is of the order 15–20 days.

To preserve the observed P gradients between stratospheric highs and lows, the above result implies that P' is altered on a similar time scale. As a result, by this argument, it appears plausible that P and R become reasonably well correlated after the first month of the experiment (Fig. 5.6).

4) "ZERO-DIMENSIONAL" BEHAVIOR (RESIDENCE TIMES)

Perhaps the simplest way to evaluate the gross behavior of a stratospheric pollutant with a sink in the troposphere is to employ the concept of "residence time." Consistent with common usage, residence time (τ_{res}) is defined here as the integrated tracer amount divided by the integrated removal rate. This is roughly the time for a tracer amount to be reduced to a factor of $1/e$ of its original value.

Fig. 5.7 presents residence times calculated from this experiment for the entire model atmosphere and for the model Northern Hemisphere. This figure shows that the model τ_{res} tends to increase systematically with time from values less than 12 months during the first half of the experiment to over 24 months during the last year or so. The model Northern Hemisphere τ_{res} shows a very large seasonal variation with large indi-

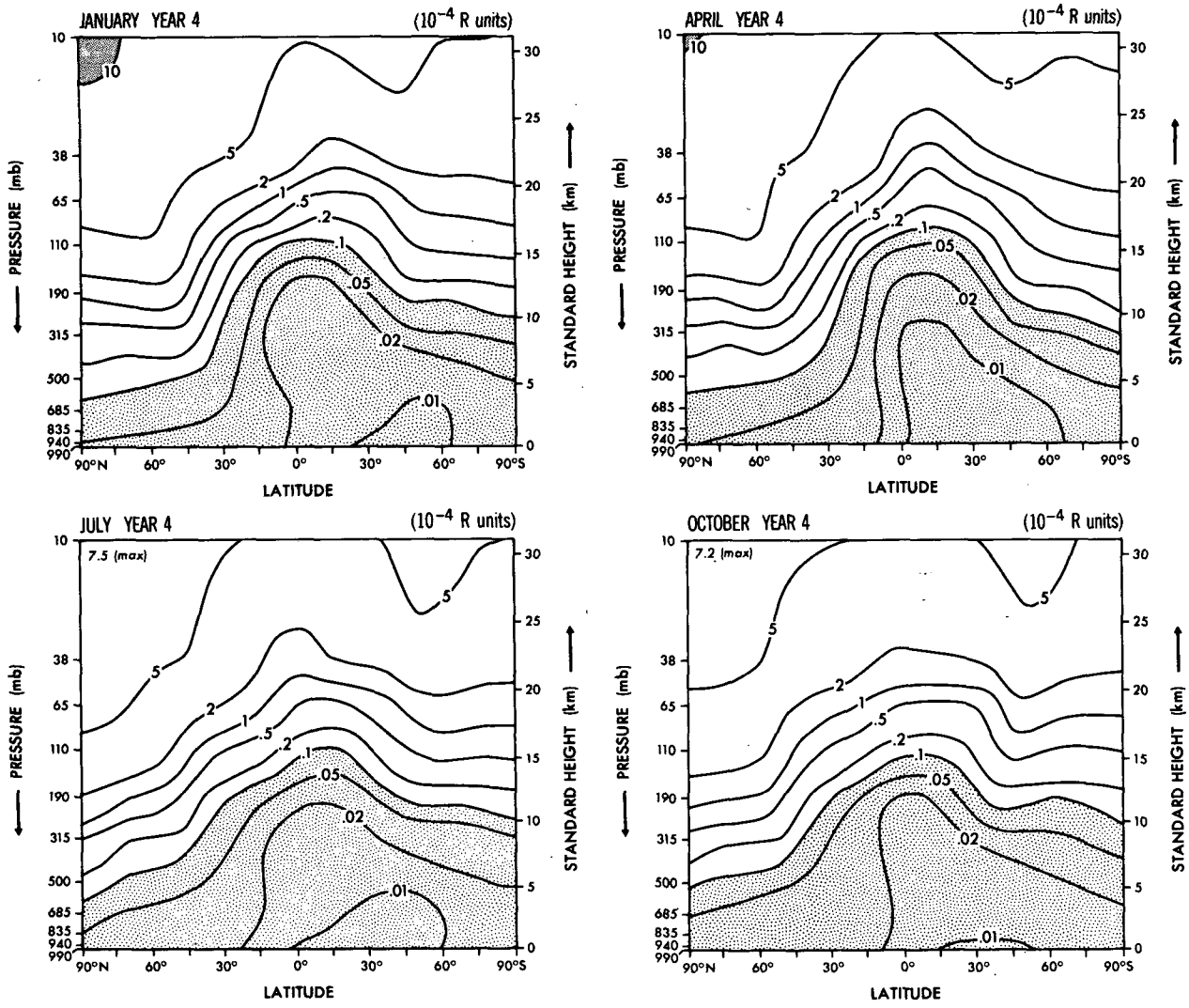

FIG. 5.1d. As in Fig. 5.1a except for year 4.

cated τ_{res} from November to January and small τ_{res} from April to July.

This large variation is not caused so much by seasonal variation in transport to the troposphere as it is by the presence of a strong seasonal variation in the interhemispheric exchange rate. During the Northern Hemisphere winter, the model net cross-equatorial tracer transport is northward. This is caused mainly by the mean meridional circulation moving from the summer to winter hemisphere in the model stratosphere (see Fig. 5.1 of MM76). As the center of gravity of the tracer gradually rises with time, this effect becomes progressively larger, as seen in Fig. 5.7. This type of seasonal dependence suggests that it may be misleading to infer true residence times from observational data which are effectively sampled only in the Northern Hemisphere (as is the case for much of the radioactivity data). In this context, it is interesting to note in Fig. 5.7 that the "observed" particulate debris residence times calculated by Machta and Telegadas (1973) fall somewhat between the model global and Northern Hemisphere values for the first year of the experiment.

The increasing stratospheric τ_{res} in Fig. 5.7 can be contrasted against the observation that the residence times for particulate debris tend to be nearly constant with time (Feely *et al.*, 1966; Telegadas and List, 1969). The data of Feely *et al.* for Sr^{90} and Mn^{54} during 1963–65 indicate constant τ_{res} of about 14–15 months, as indicated by the bar in Fig. 5.7. Thus, the residence times of this experiment are only consistent with the particulate radioactive debris residence times for about the first year.

On the other hand, Feely *et al.* (1966) indicate that the apparent excess $C^{14}O_2$ (amount above background $C^{14}O_2$) residence times for the same period increase from around two years during the first year to more

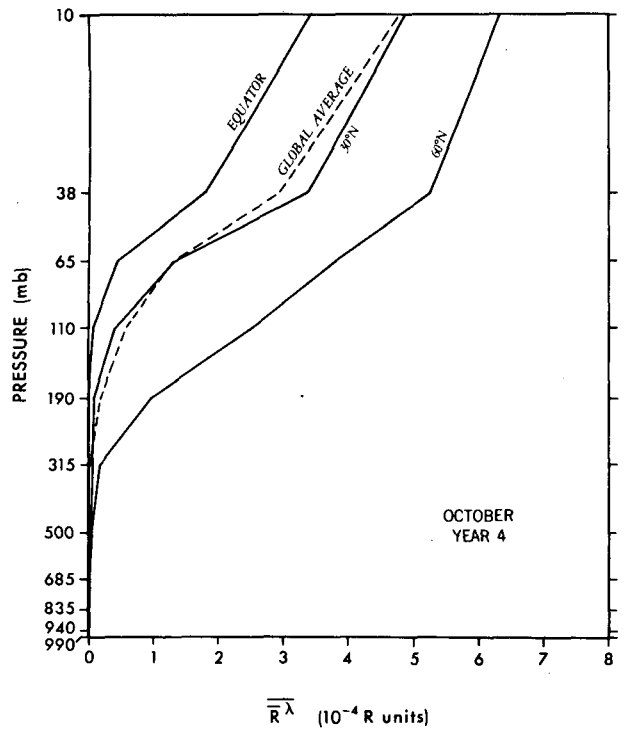

FIG. 5.2. Selected vertical profiles of zonal mean tracer mixing ratio (10^{-4} R units) for October year 4. Linear units clarify distinct change in vertical tracer gradient above zonal-mean tropopauses.

than four years several years later (see triangles in Fig. 5.7). Thus, the increasing τ_{res} behavior shown in Fig. 5.7 for this experiment falls between the τ_{res} behavior obtained from particulate radioactive debris and $C^{14}O_2$. Such a result appears consistent in the sense that settling would tend to keep the center of gravity of the particulate debris in the lower stratosphere as time progresses. Furthermore, one would expect a greater increase of apparent residence time for the $C^{14}O_2$ data than for this experiment because of the progressively increasing importance of back transport of $C^{14}O_2$ from the troposphere as time progresses. This is because with increasing time, typical tropospheric $C^{14}O_2$ mixing ratios become progressively more significant relative to typical stratospheric values. The data listed in Johnston *et al.* (1976) indicate that for $C^{14}O_2$, this difference becomes less than one order of magnitude during the second year following cessation of testing.

The increase of residence time later in the experiment seen in Fig. 5.7 leads to the question of how the residence time depends on the average vertical distribution of the tracer. Fig. 5.8 shows residence time calculated over one-year intervals (to eliminate seasonal effects) plotted against yearly global averages of the height of the average center of mass of the tracer (same amount above as below a point). This figure shows that for this experiment there is a nearly linear relationship between residence time and mean center of gravity of the tracer. The calculated average rate of change of τ_{res} with height is between 0.3 and 0.4 year km^{-1}. Note in Fig. 5.8 that the empirical two-dimensional model of Fabian and

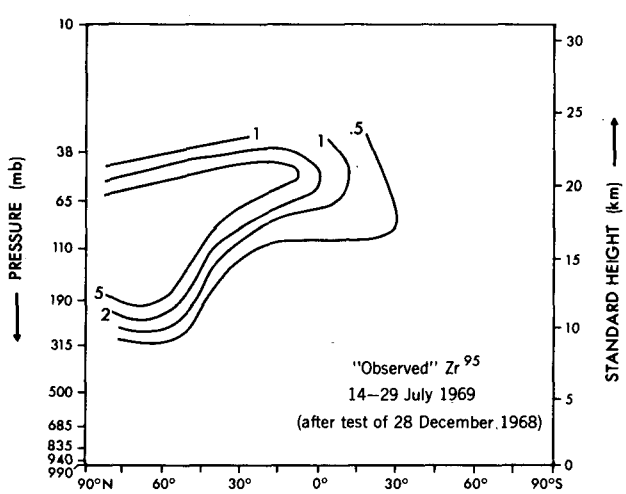

FIG. 5.3. Approximate observed zonal mean distribution of Zr^{95} (corrected for radioactive decay to 29 September 1969) for 14–29 July 1969, following nuclear test of 28 December 1968. Data source: Machta and Telegadas (1973). Units: per standard cubic meter (equivalent to mixing ratio).

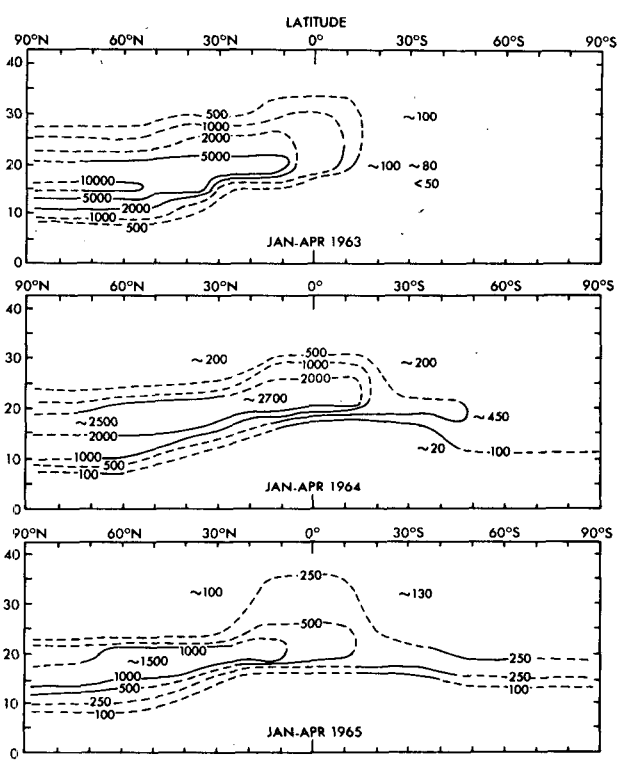

FIG. 5.4. Approximate observed zonal mean distribution of Mn^{54} (corrected for radioactive decay) for January–April periods in 1963, 1964 and 1965. Data source: Feely *et al.* (1966). Units: 10^{-3} disintegrations per standard cubic foot (equivalent to mixing ratio).

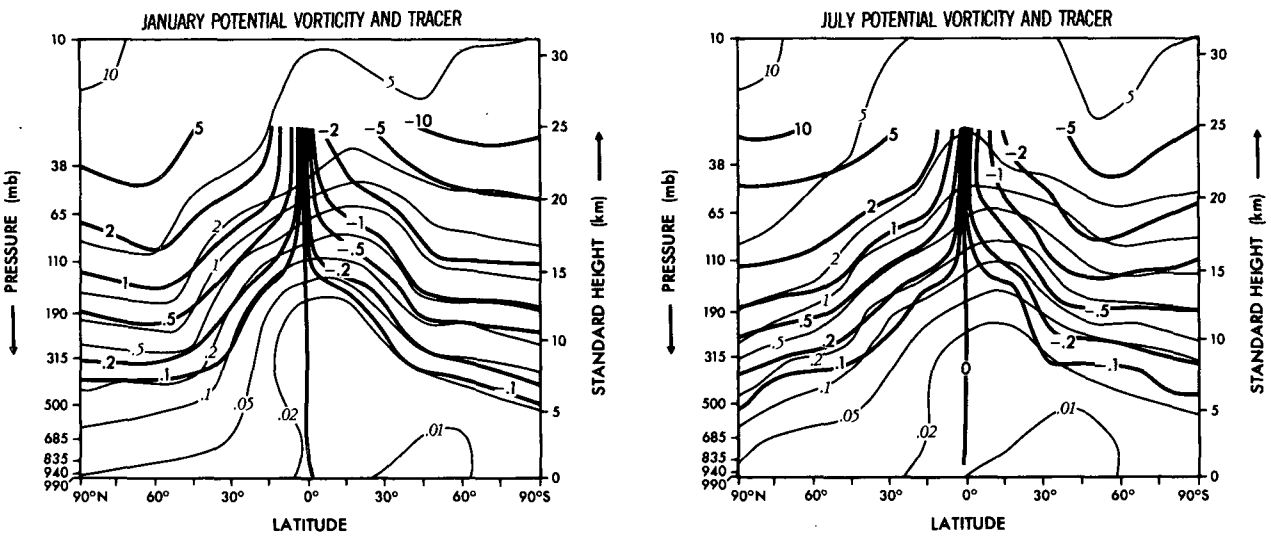

FIG. 5.5. Isentropic potential vorticity of the January and July zonal mean structure (heavy lines, 10^{-6} m s K kg^{-1}) and zonal mean tracer (thin lines 10^{-4} R units).

Libby (1974) suggests a significantly smaller altitude dependence of τ_{res}. On the other hand, Hunten (1975) indicates a value of about 0.65 year km^{-1} based on the behavior of $C^{14}O_2$.

This result provides an interesting perspective on the question of why the apparent τ_{res} for $C^{14}O_2$ was significantly larger than for the particulate debris in early 1963 when the effect of particle settling would probably not have had time to become significant. The data of Fig. 5.8 suggest that if the center of gravity of the $C^{14}O_2$ cloud had initially been 2.5–3 km higher than the particulate debris cloud, the discrepancy would be explained. Such an inference is consistent with the arguments of Telegadas and List (1969) and Chang (1976) that $C^{14}O_2$ should have had a higher center of gravity in early 1963 than the particulate debris due to expected enhancement of C^{14} relative to fission products in the highest yield tests of the 1961–62 series. On the other hand, Feely *et al.* (1966) and Johnston *et al.* (1976) suggest that particle settling is sufficient to explain the τ_{res} differences by a preference for fission products to be associated with large particles, and hence, larger than expected settling speeds.

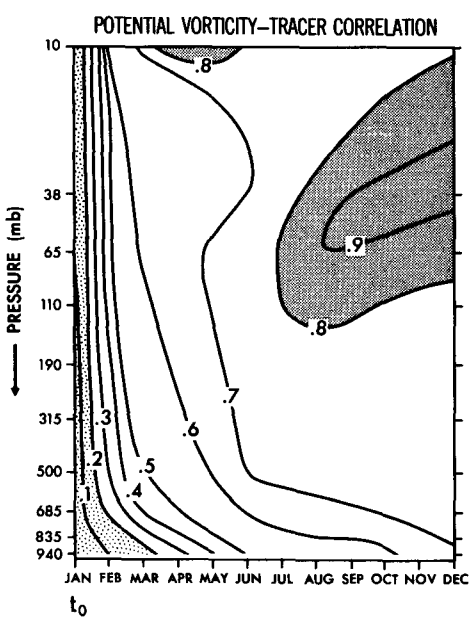

FIG. 5.6. Instantaneous linear correlation coefficient between model tracer and isentropic potential vorticity. Correlation is calculated for each model level at the first of each model month.

Comparison of this experiment with observed behavior suggests that particle settling is very important over longer times, but that the $C^{14}O_2$ debris was probably present at somewhat higher altitudes than the particulate debris in early 1963. This inference is consistent with the observations of Telegadas and List (1969) that τ_{res} for $C^{14}O_2$ and particulate debris were reasonably similar during 1960 (a period following a nuclear test series where high yield devices were not detonated), but were quite different in 1963 following detonation of a mix of high- and low-yield devices.

5) Interhemispheric tracer transport

Another quantity which can provide a simple evaluation of the model performance against observation is the rate of exchange between hemispheres as evidenced by the total tracer amounts in each hemisphere. Fig. 5.9 shows the time evolution of the model ratio of mean Northern Hemisphere tracer to mean Southern Hemisphere tracer ($\overline{R}^{N.H.}/\overline{R}^{S.H.}$). As expected, this ratio decreases with time, first rapidly and then gradually. Consistent with the Northern Hemisphere residence time calculations in Fig. 5.7, there is a noticeable seasonal variation in this quantity.

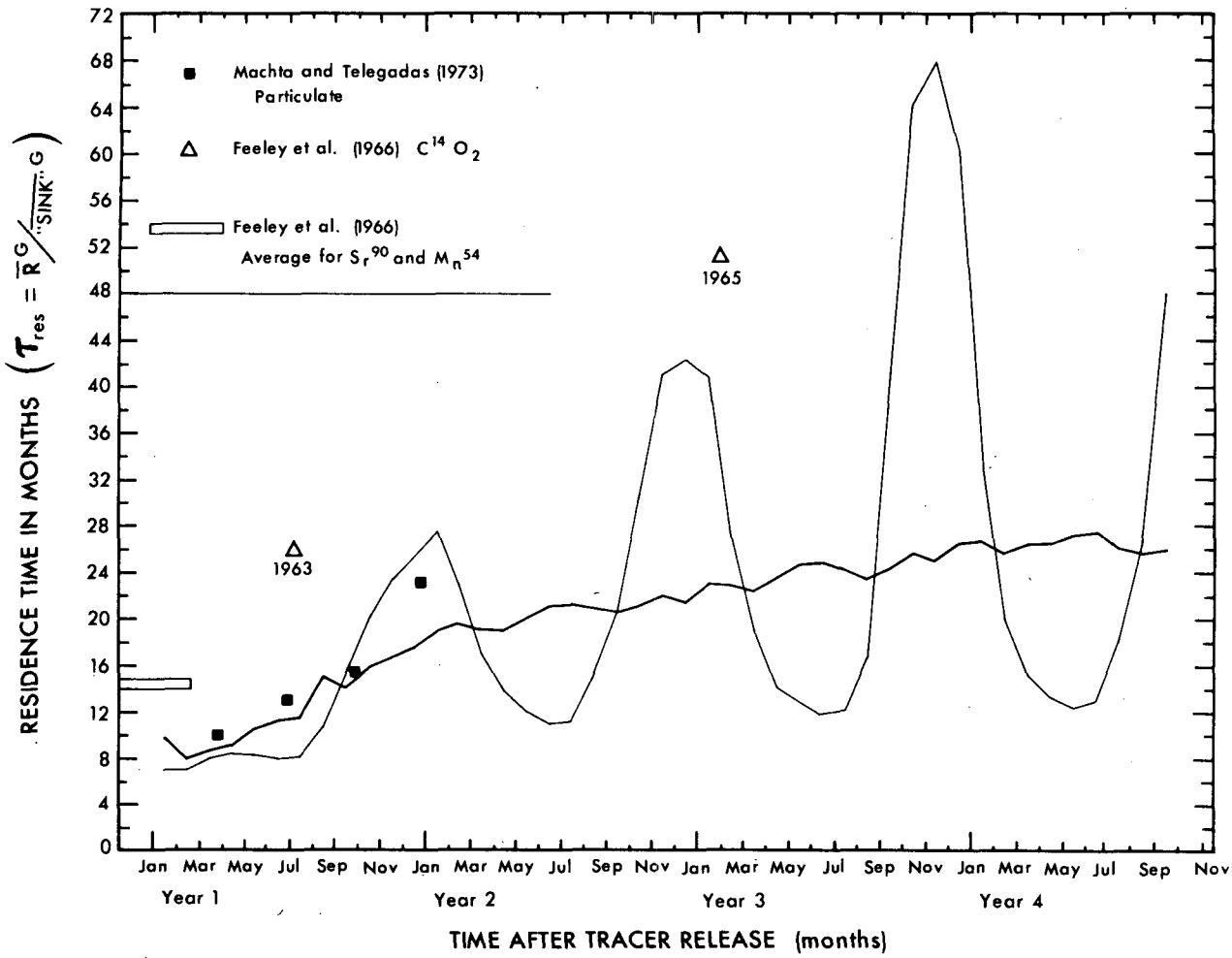

FIG. 5.7. Time evolution of model residence time (τ_{res}) in months. Heavier solid line is global residence time; thin solid line is Northern Hemisphere residence time. Corresponding observed data for $C^{14}O_2$ and particulate tracers are given as indicated.

For sake of comparison, observational values of the same quantity are plotted in Fig. 5.9 (solid circles) using the 1963–1966 $C^{14}O_2$ data of Telegadas (1971). The $C^{14}O_2$ data shows much smaller values in early 1963 because of the presence of excess $C^{14}O_2$ in the Southern Hemisphere from previous nuclear detonations. The longer term evolution of $\bar{R}^{N.H.}/\bar{R}^{S.H.}$ for $C^{14}O_2$ shows similar behavior to the model experiment, but with a smaller seasonal variation. Whether or not this is a model defect is not clear. The model exhibits a somewhat higher center of gravity than the observed $C^{14}O_2$ data because of the relatively rapid tropospheric removal of the model tracer. Thus, the tracer experiment may show a larger susceptibility to the seasonal variation in the cross-equatorial meridional circulation discussed in the previous section.

It is also interesting to note that, although Fig. 5.9 shows that $\bar{R}^{N.H.}/\bar{R}^{S.H.}$ decays slowly with time, the time of largest simulated tracer amount in the Southern Hemisphere is September during the first year. After that, the average Southern Hemisphere tracer amount decays with an apparent residence time of about 3 years, nearly twice the apparent value typical of the model Northern Hemisphere, as seen in Fig. 5.7. This is, of course, due to the transport of tracer into the Southern Hemisphere.

b. Large-scale transport phenomena in the model stratosphere

1) ZONAL MEAN BALANCES

As reviewed in the Introduction, opinion has varied widely over the years as to which are the dominant mechanisms of meridional tracer transfer in the stratosphere. One way to shed light on this question is to analyze the model data in terms of the processes which can lead to changes in the zonal mean tracer mixing ratio, even though the integration itself includes zonally asymmetric effects. This allows a more straightforward comparison with the usual general circulation statistics, dynamical theories, observed tracer behavior and two-dimensional models. Also, such an approach allows discussion of transport processes in rather precise terms.

As will be discussed later, this type of formulation does not always lead to the most meaningful physical understanding of the tracer transport process. However, in many cases, the insights obtained by this type of analysis are highly revealing.

By transforming Eq. (3.7) into pressure coordinates, zonal averaging, and manipulating, one obtains

$$\underset{(E_H)}{\frac{\partial \overline{R}^{\lambda}}{\partial t}} = \underbrace{-\frac{1}{a\cos\phi}\frac{\partial}{\partial\phi}\overline{v'R'}^{\lambda}\cos\phi}_{(E_H)} \underbrace{-\frac{\partial}{\partial p}\overline{\omega'R'}^{\lambda}}_{(E_V)} \underbrace{-\frac{\overline{v}^{\lambda}}{a}\frac{\partial \overline{R}^{\lambda}}{\partial\phi}}_{(M_H)} \underbrace{-\overline{\omega}^{\lambda}\frac{\partial \overline{R}^{\lambda}}{\partial p}}_{(M_V)} + \overline{\text{DIFFUSION}}^{\lambda} + \overline{\text{FILLING}}^{\lambda} + \overline{\text{SOURCES}}^{\lambda} - \overline{\text{SINKS}}^{\lambda} + \overline{\text{RESIDUAL}}^{\lambda}. \quad (5.3)$$

The terms in Eq. (5.3) have the following physical interpretations in terms of their influence on the time rate of change of $\overline{R}^{\lambda}$ (net tendency):

- (E_H) convergence of horizontal eddy tracer flux
- (E_V) convergence of vertical eddy tracer flux
- (M_H) horizontal advection of $\overline{R}^{\lambda}$ by the mean meridional circulation
- (M_V) vertical advection of $\overline{R}^{\lambda}$ by the mean meridional circulation.

The term $\overline{\text{RESIDUAL}}^{\lambda}$ represents the computational imbalance which can result in the calculations due to sampling error, numerical inconsistencies and transformation from σ to p coordinates. As pointed out by Mahlman and Moxim (1976), the error due to the latter effect can be particularly serious when terms involving vertical motion are important in the balances (M_V or E_V). All analyses shown here are performed according to the improved scheme outlined in that paper. The remaining terms in Eq. (5.3) are zonal averages on p surfaces of the terms as described in Section 3b.

Some early aspects of this analysis were presented by Mahlman (1973b). For sake of completeness, some of those results are included as part of this discussion. To provide an understanding of the seasonal effect on the balances, the months January, April, July and October are chosen for presentation.

Lower stratospheric balances at 65 mb for the indicated months are given in Fig. 5.10. Note that in Fig. 5.10 and subsequent balance illustrations, the M_H and M_V terms are combined for simplicity, as are the E_H and E_V terms. However, the individual components which locally dominate the combined mean or eddy effect are indicated on the figure.

The balances for January year 1 at 65 mb in Fig. 5.10 indicate a strong response to the initial tracer field. Very pronounced increases to the south of the original field are due mainly to E_H. The instantaneous charts given in Mahlman (1973b) show that this flux convergence is simply due to southward advection of the initial tracer out of the Aleutian anticyclone where it was originally placed. The two-cell meridional circulation is acting to move air horizontally back toward the source region (see MM76, Fig. 5.1), leading to decreases by M_H. The convergence and concomitant descending motion act to increase the tracer near the source region, but the eddy removal tends to overwhelm it. At this early stage, $\overline{\text{DIFFUSION}}^{\lambda} + \overline{\text{FILLING}}^{\lambda}$ plays a significant role because of the extreme gradients associated with the impact of the stratospheric motion on the initial tracer field.

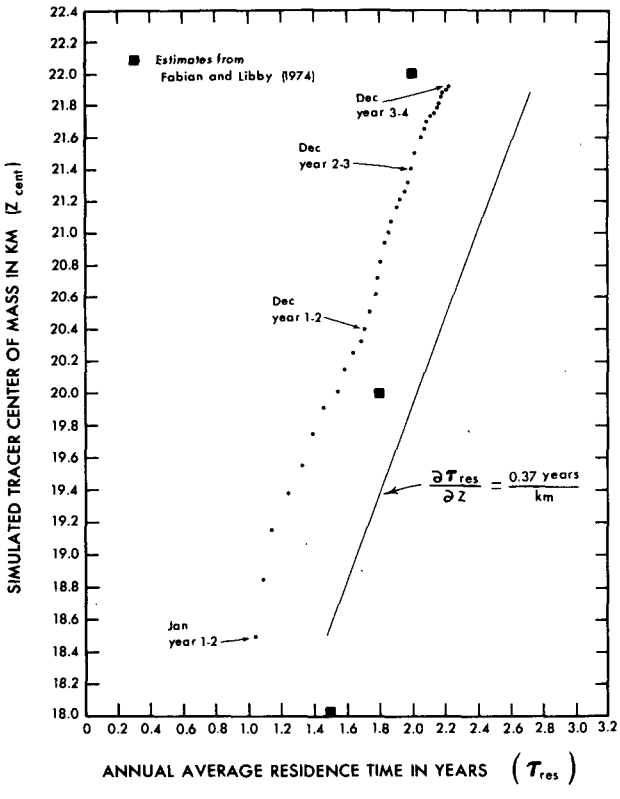

FIG. 5.8. Global annual mean residence time (τ_{res}) versus tracer average center of mass. Dates give position of the center of mass as the experiment evolved.

Fig. 5.10 shows that for April and succeeding months, the magnitudes of removal from the source region are considerably smaller and less localized than in January. The April removal is still dominated by horizontal eddies with weak opposition by M_V. This eddy activity is associated with the simulated weakening of the winter polar vortex and transition to summertime circulation. Note in Fig. 5.10 the importance of the eddies in producing the protrusion of $\overline{R}^{\lambda}$ into the Southern Hemisphere stratosphere as seen in Fig. 5.1a. In low latitudes the net eddy effect is positive. However, E_V is negative with a magnitude about that of the meridional circulation effect. This removal results from

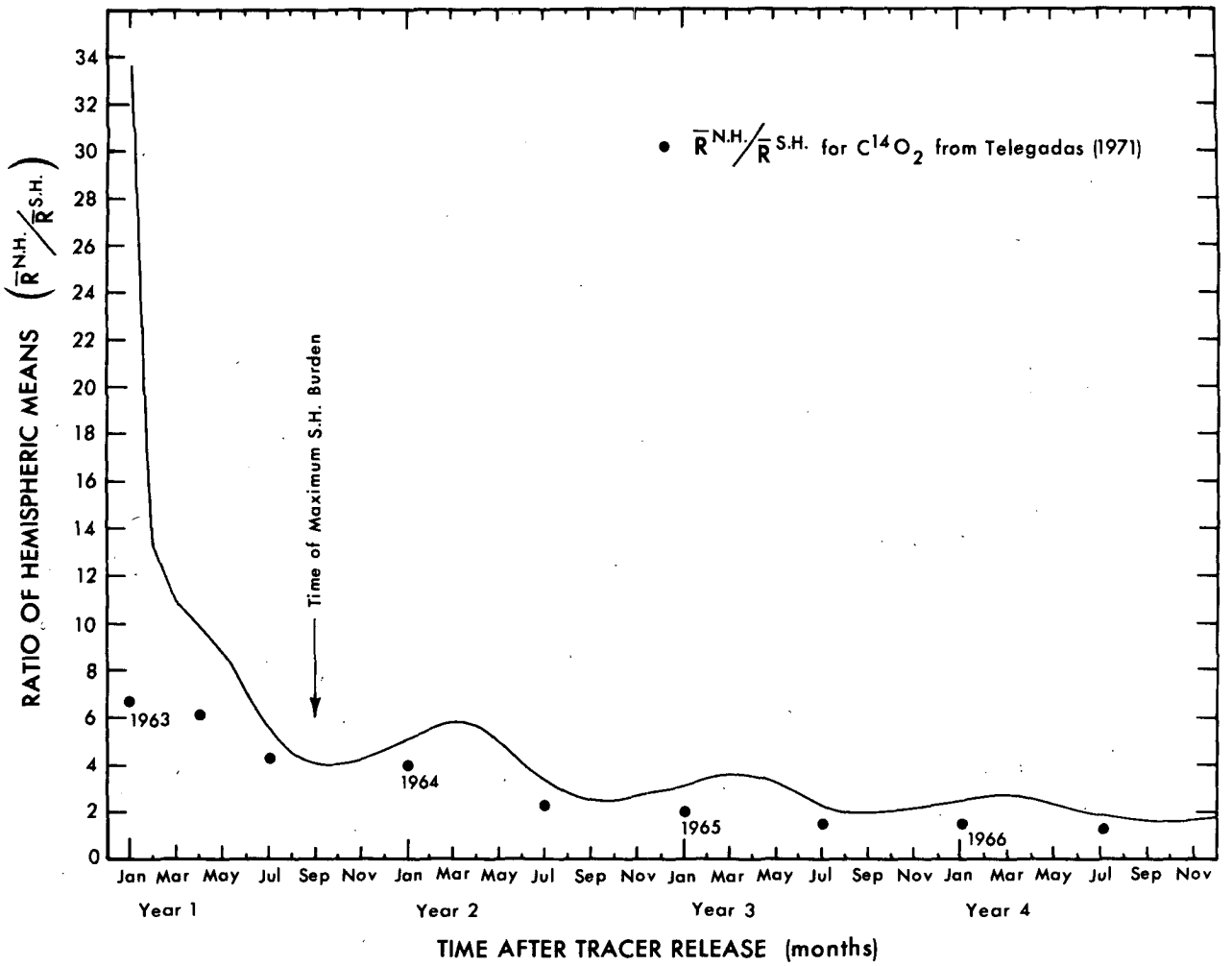

FIG. 5.9. Time evolution of model ratio of Northern Hemisphere mean tracer to Southern Hemisphere mean tracer. Observed $C^{14}O_2$ data are given as indicated. Note presence of significant amounts of $C^{14}O_2$ in the Southern Hemisphere in early 1963.

vertical eddy flux away from the 65 mb level in both vertical directions.

In July, the meridional circulation is quite weak and the tracer tendencies are mainly affected by E_H and E_V in various combinations. Note the strong increase of tracer near the North Pole due to E_H. This process is of importance in helping to establish the evolving poleward-downward slope of $\bar{R}^{\lambda}$ seen so clearly in Fig. 5.1.

The October year 1 balances at 65 mb are dominated by the onset of the winter circulation which sets up a marked degree of cancellation between the mean cell and eddy terms in high northern latitudes. This phenomenon has been previously observed in heat and tracer balances in both observational and numerical studies as discussed in the introduction. The effect is quite clear in the dynamical balances of this model as pointed out in MM76, and is of significant interest from a number of perspectives. Some aspects of its theoretical interpretation will be presented in the following section.

An immediate inference is that mean cell and eddy transfers do not act independently of each other under such circumstances. Also, the zonal mean balance approach utilized here may not yield the maximum physical insight in these situations.

In the mid- and high-latitude region where the degree of cancellation is large, the smallness of the net tendency relative to the main terms is noteworthy. Nevertheless, an important net tracer transfer is taking place under these circumstances. Note that a buildup of tracer is occurring at about 60–65°N, near the crossover point where the M and E terms are changing sign.

At other latitudes the degree of the mean cell-eddy cancellation is also pronounced. In fact, the linear correlation coefficient between the M and E terms is -0.996 for the entire 65 mb level. However, south of the equator, the tendency is comparable in magnitude with the individual terms. The net effect is to produce a slow removal of tracer over a broad range of latitude.

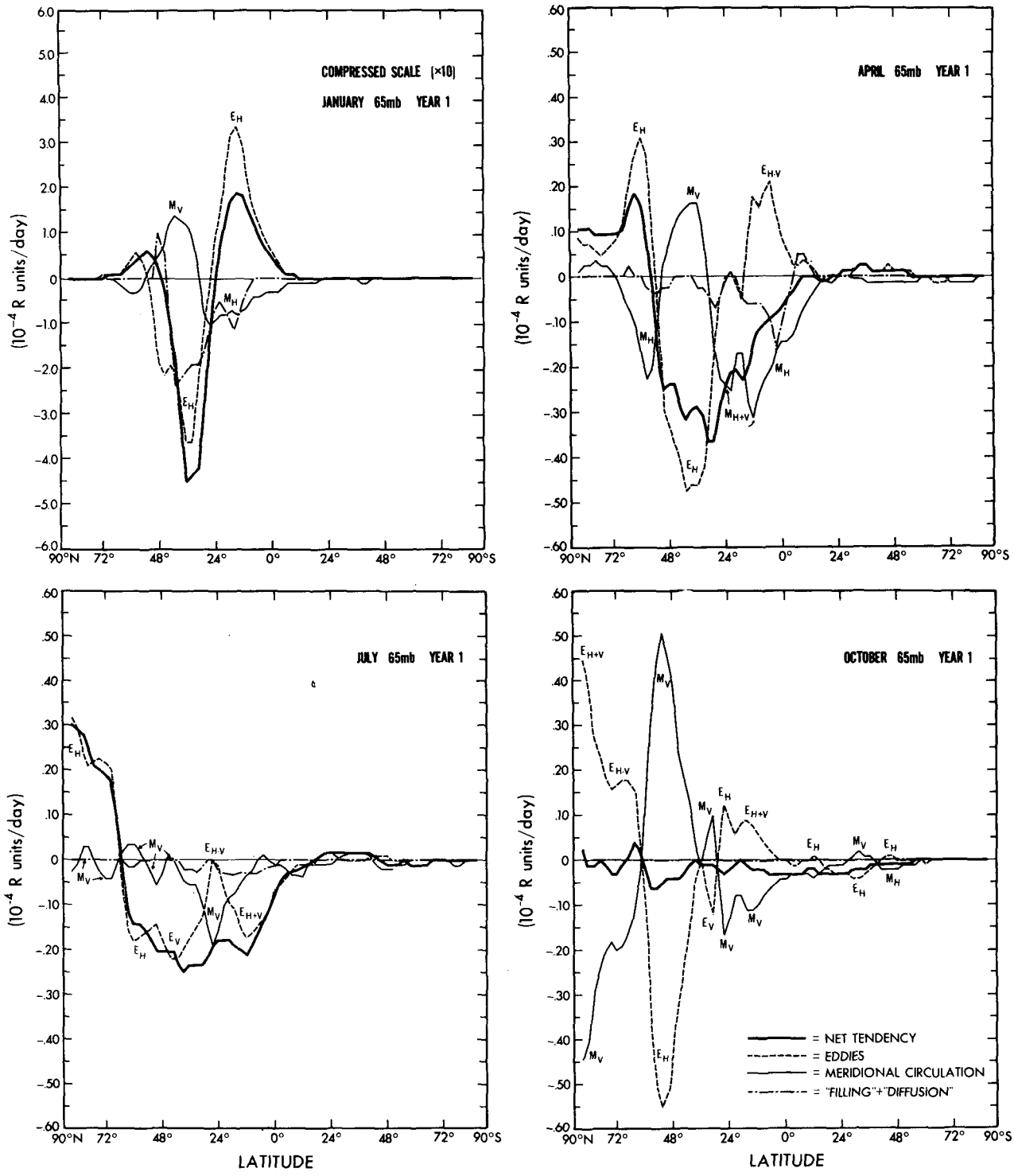

FIG. 5.10. Mechanisms leading to changes in the zonal mean mixing ratio (10^{-4} R units day^{-1}) at 65 mb for indicated months during year 1. Terms are as given in Fig. 5.3. Legend for lines is given at lower right. The notations E_H, E_V, M_H or M_V mean that for the given mean (M) or eddy (E) contribution to the net tendency ($\partial \bar{R}^{\lambda}/\partial t$), either the vertical ($V$) or horizontal ($H$) part dominates there as indicated. Note change of scale for January.

The balances for the first year at 10 mb are shown in Fig. 5.11. As pointed out in MM76, the circulation is somewhat distorted at 10 mb in this simulation, probably because of the coarse vertical resolution there and the use of the "lid" vertical boundary condition in the GCM. Nevertheless, they showed that in spite of these

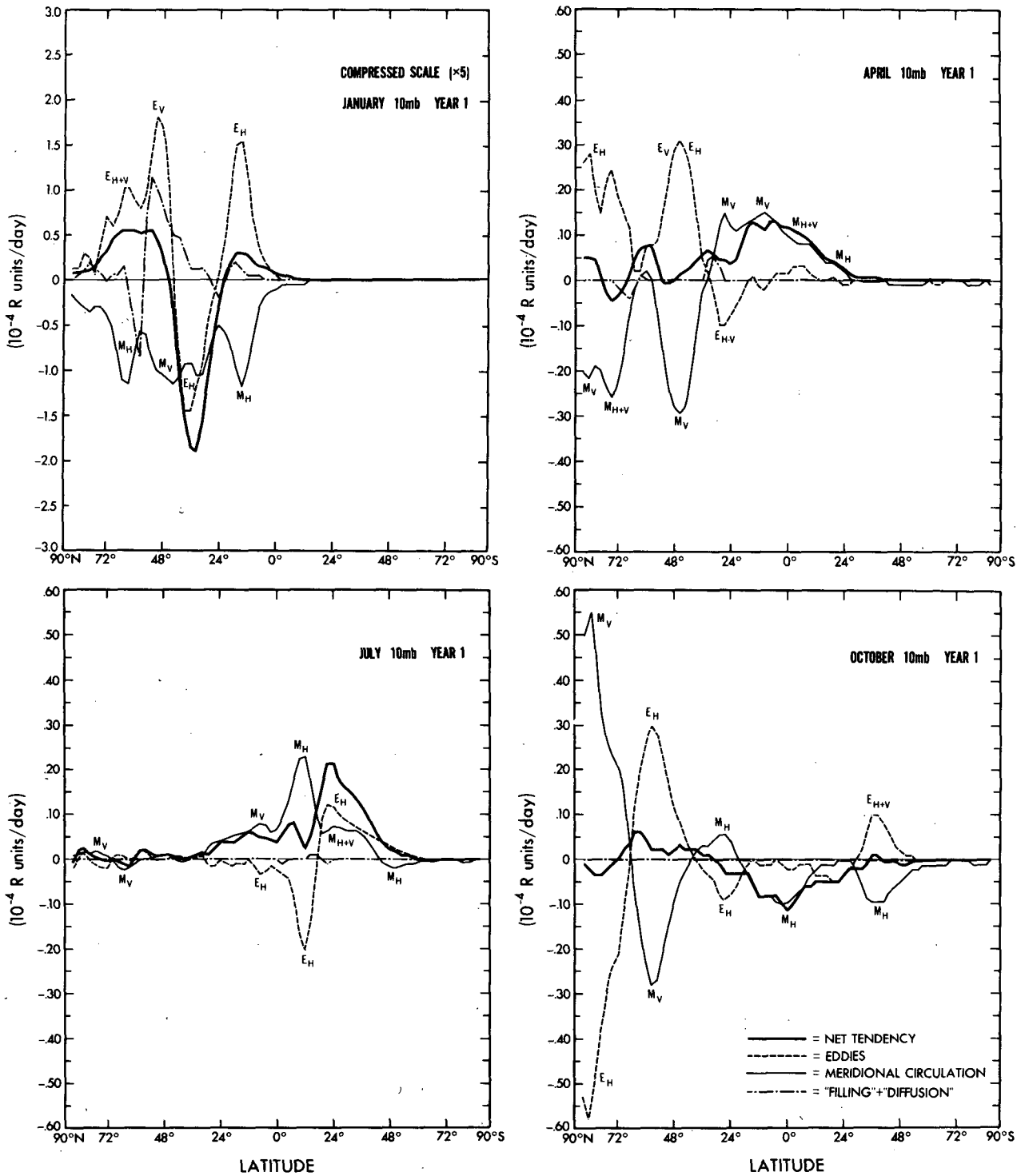

FIG. 5.11. As in Fig. 5.10 except at 10 mb, year 1.

limitations, the 10 mb behavior is noteworthy because of the pronounced seasonal variations which appear there in the simulation.

The January 10 mb balances in Fig. 5.11 show strong removal from the source region similar to that seen at 65 mb in Fig. 5.10. In this case, the two-cell meridional circulation is acting to decrease the tracer everywhere, with the effect of M_H being atypically large due to the strong horizontal gradient of $\overline{R}^{\lambda}$. Poleward of the $\overline{R}^{\lambda}$ maximum (Fig. 5.1a), tracer is being brought up from lower levels through the effect of E_V.

During April of year 1, Fig. 5.11 shows a strong degree of mean cell-eddy cancellation, but in a form rather different than what one might expect. The two-cell meridional circulation is leading to removal of tracer in both mid- and high-latitudes. The removal due to descending motion in mid-latitudes is consistent with the expectation for a tracer which decreases with increasing height. However, at the pole, the rising mean cell leads to $\overline{R}^{\lambda}$ decreases. Fig. 5.1a reveals that at the pole, the 10 mb mixing ratio is somewhat larger than at lower levels. Consequently, the ascending meridional circulation is advecting lower $\overline{R}^{\lambda}$ values upward, thus leading to the observed decreases through M_V. These higher values at the 10 mb north polar region originally occurred because the stronger circulation in the January–March period led to larger poleward tracer fluxes there than at lower levels.

In lower latitudes, the April 10 mb balances show particularly strong $\overline{R}^{\lambda}$ increases. This increase is mainly due to a seasonal change in the meridional circulation, with rising motion in the northern subtropics and southward movement across the equator (see MM76, Fig. 5.1). This effect produces an upward and southward advection of $\overline{R}^{\lambda}$ which is clearly reflected in the tendency field. Notice that the degree of mean cell-eddy cancellation is much smaller in low latitudes. An explanation of the July 10 mb balances shown in Fig. 5.11 has already been given in some detail in Mahlman (1973b), with a synoptic interpretation included. Those results showed that high latitudes are nearly devoid of tracer transfer due to the presence of the nearly symmetric easterly regime at this time. In low latitudes, the meridional circulation again acts to move tracer upward and southward producing significant tracer increases there. At about 10–15°S, $\overline{v}^{\lambda}$ begins to weaken, but the subtropical anticyclones act to remove tracer from the region and transport it further southward, leading to the large $\overline{R}^{\lambda}$ increase due to E_H at about 25°S.

The October 10 mb balances show a large degree of cancellation between mean cell and eddy effects similar to those at 65 mb for the same month. The sense of the cancellation is opposite to that shown in the 65 mb October balances. This is because the vertical gradient of $\overline{R}^{\lambda}$ at 10 mb is opposite that at the 65 mb level. Note, however, that the mixing ratio is again increasing near the point of crossing of the two large nearly cancelling terms. Also, the cancellation is mainly between the E_H and M_V terms.

In lower latitudes, the $\overline{R}^{\lambda}$ tendency is now negative in sharp contrast to the large positive tendencies shown in Fig. 5.11 for April and July. This is associated with the seasonal reversal of the meridional circulation so that the flow is into the winter hemisphere. Also, for the first time, the Southern Hemisphere tracer amounts are large enough to produce observable effects there. The M_H term is large because of the large horizontal gradient of $\overline{R}^{\lambda}$ near 40–45°S as seen in Fig. 5.1a.

Although the advecting wind fields in this model do not change from year to year, the dominant transport phenomena do change when the overall tracer distribution has evolved into a different state. This can be illustrated by examining the balances for the same months as in Fig. 5.10 and 5.11, but for the third year of the experiment.

Fig. 5.12 shows the balances for year 3 at 65 mb. The January year 3 balances, in marked contrast to the January year 1 balances, show a very high degree of mean cell-eddy cancellation. In fact, the mean cell-eddy correlation coefficient is -0.995, while the correlation between E_H and M_V is -0.901. In the Northern Hemisphere, these balances are remarkably similar to that shown by Mahlman (1973b) for January using the same model, but applied to a vertically stratified "ozone-like" tracer. This suggests that the vertical stratification of tracer in the present experiment (established by the initial SOURCE and maintained by the tropospheric sink) is the dominant effect in controlling the nature of the zonal mean balances in the model winter season. Although the tracer is slowly diminishing with time in midlatitudes, during winter this loss is locally compensated by an extra net downward flux of tracer. This extra flux is excited by the action of the model planetary-scale disturbances as described earlier in MM76.

In April, Fig. 5.12 shows that significant negative tendencies are beginning to occur. This tracer removal is apparently due to the weakened planetary-scale disturbances as evidenced by the reduced degree of mean cell-eddy cancellation as compared to the January balances.

The July year 3 balances in Fig. 5.12 show a remarkable change in structure. Note the large removal of tracer poleward of 60°N by E_H. In this case, there is almost no cancellation between mean cell and eddy effects. The large tracer removal in high latitudes is opposite to the behavior for 65 mb July year 1 shown in Fig. 5.10. This is because the highest mixing ratios are near the pole in year 3, while they were still largest in midlatitudes during July of year 1 (see Figs. 5.1a and 5.1c). At other Northern Hemisphere latitudes, this reduction of the cancellation is less evident. Nevertheless, the zonal mean tracer tendencies are now decidedly produced by eddy effects. Some of the reasons behind this drastically contrasting seasonal transport behavior will be discussed in the following section. In the Southern Hemisphere, the balances are also very different than presented in Fig. 5.10 for July year 1. During the first year, the tracer amounts were very small and the transport was dominated by very large horizontal tracer gradients. However, Fig. 5.12 shows that the Southern Hemisphere July balances are

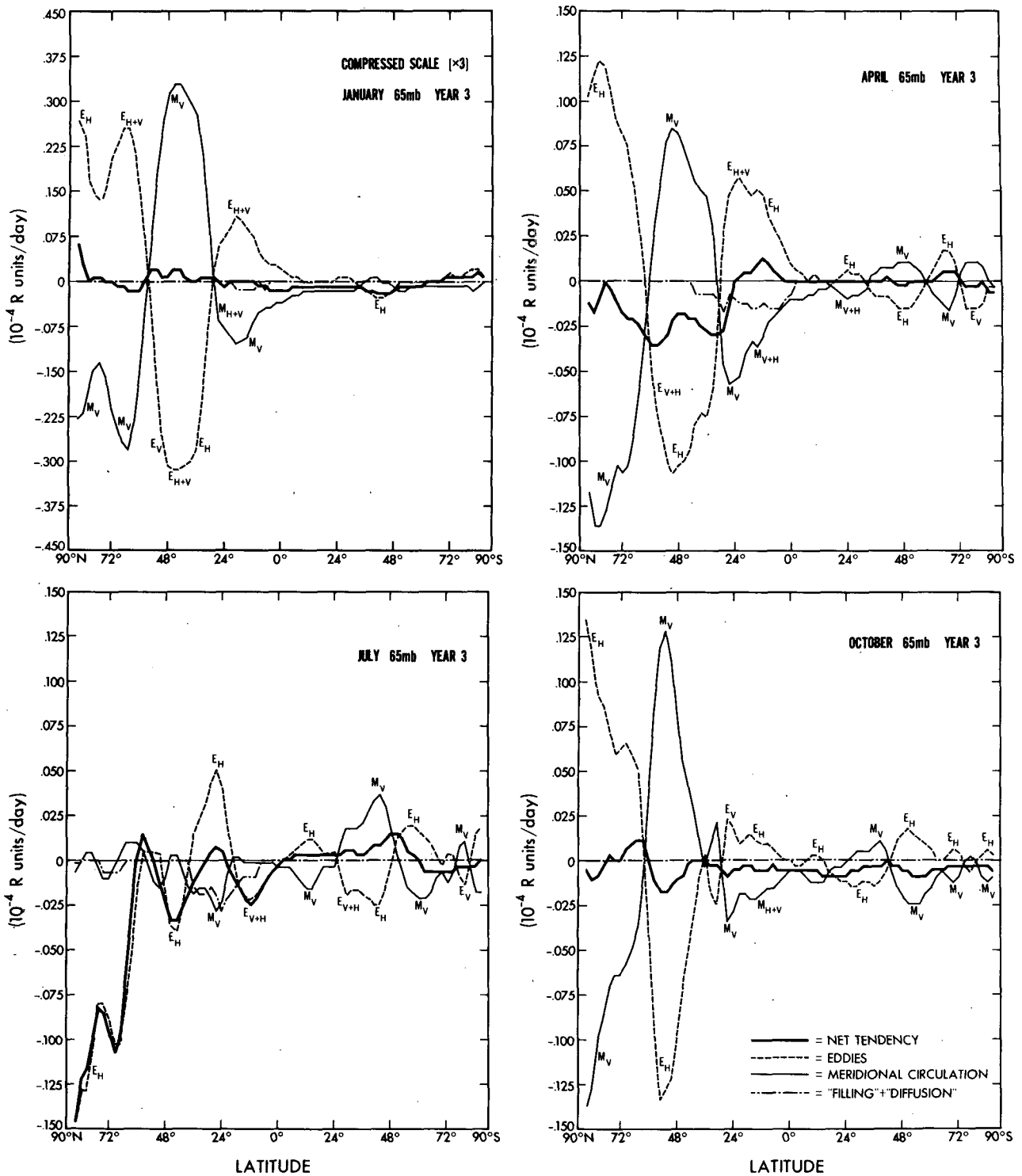

FIG. 5.12. As in Fig. 5.10 except at 65 mb, year 3.

beginning to show a substantial degree of mean cell-eddy cancellation. Again the largest buildup of tracer occurs at the crossover point between the opposing mean cell and eddy contributions. Note that this point is near 45°S rather than near 60° as it is in the Northern Hemisphere. As pointed out in MM76, the winter planetary wave amplitudes in this GCM experiment are considerably weaker in the Southern Hemisphere with

a higher fraction of the wave activity in the transient disturbances. They argued that these differences are probably related to the presence of major mountain ranges in the Northern Hemisphere.

The October year 3 balances at 65 mb for the Northern Hemisphere are very similar to that shown for October year 1 in Fig. 5.10. This suggests that 10 months following the release of the source is sufficient for a tracer to "forget" the specific details of its initial distribution. It is then essentially controlled in its transport by the large-scale dynamics of the stratosphere and the long-term effect of the tropospheric sink. In the Southern Hemisphere, the degree of mean cell-eddy cancellation is smaller than that seen in July. This is because the planetary-scale disturbances have weakened during the onset of spring with its increased high-latitude radiative heating. An interesting aspect of this transition is that its relative effect on $\overline{R}^{\lambda}$ is much smaller than during the model Northern Hemisphere spring. The cause of this difference is presumably related to the presence of much larger stationary disturbances in the model Northern Hemisphere (MM76). When these large stationary disturbances break down, they leave as remnants large departures from zonal symmetry in the wind field and the tracer field. The tracer is then subject to significant redistribution, both zonally and meridionally.

Fig. 5.13 shows various balances at 10 mb for year 3. For January the two-cell meridional circulation is leading to $\overline{R}^{\lambda}$ increases poleward of 45°N and decreases elsewhere. The polar behavior results because $\overline{R}^{\lambda}$ decreases upward and southward (the largest $\overline{R}^{\lambda}$ values at this time are at 38 mb near the pole). Thus, both M_V and M_H act to increase $\overline{R}^{\lambda}$. At the lower latitudes, $\overline{v}^{\lambda}$ is positive, while rising motion is occurring in the Southern Hemisphere subtropics. The pronounced removal by M_H around 12°N is partly due to the strong meridional gradients of $\overline{R}^{\lambda}$ there. The Northern Hemisphere eddy terms can be directly related to the presence of the Aleutian anticyclone seen so clearly in Fig. 4.2. The strong $\overline{R}^{\lambda}$ increase by E_H near 12°N is caused by some of the tracer-rich air moving around the base of the Aleutian high and getting caught in the simple easterly flow in low Northern Hemisphere latitudes. The $\overline{R}^{\lambda}$ removed by E_V at around 60°N is related to the presence of pronounced sinking motion in the eastern Siberia region to the west of the Aleutian high and on the cyclonic shear side of the simulated polar night jet stream evident in Fig. 4.2 (see MM76, Section 10).

For April at 10 mb, Fig. 5.13 shows that the Northern Hemisphere removal is considerably smaller than for January. Note also that the large degree of mean cell-eddy cancellation seen near 12°N in January has virtually disappeared. This is related to the weakening of the midwinter Aleutian anticyclone system and the reversal of $\overline{v}^{\lambda}$ noted earlier. In the Southern Hemisphere, a significant tracer buildup is occurring near 45–50°S due to the action of the midwinter planetary-scale disturbances, as pointed out previously.

In July, the north polar regions show the tendency resulting almost completely from E_H. During July in the real atmosphere, there would be essentially no nonzonal features present in the balances there. The reason for this E_H effect is that the simple, almost zonally symmetric easterly regime does not become completely established in the model until about 10 July. The Southern Hemisphere balances show continued buildup of tracer in midlatitudes. Note the complexity of the balances in that E_H, E_V, M_H and M_V all produce significant transport effects there. Another interesting feature is that the balances between E_H and M_H at 12°S are opposite to that shown for July year 1 in Fig. 5.11, although both show a positive tendency. A look at Fig. 5.1 shows that the meridional gradient of $\overline{R}^{\lambda}$ has changed sign by year 3 and that higher mixing ratios are now to the south of this region. This is the case even though Fig. 5.9 shows that there is still more than twice as much tracer in the Northern Hemisphere than in the Southern Hemisphere at this time.

The Northern Hemisphere October year 3 balances in Fig. 5.13 are especially interesting because the sense of the mean cell-eddy compensation is opposite to that shown in Fig. 5.11 for October year 1. This is because $\overline{R}^{\lambda}$ now increases with height everywhere in this region, while the opposite was the case in October year 1. Note that the $\overline{R}^{\lambda}$ removal is comparatively large there. It is this removal which is helping supply the gradual buildup near 60°N at 65 mb for the same period (see Fig. 5.12). In the Southern Hemisphere, a significant tracer removal is occurring at about 60°S. This is apparently related to the spring weakening of the winter disturbances which led to the tracer buildup in July as seen in Fig. 5.13.

2) THEORETICAL INTERPRETATION OF ZONAL MEAN BALANCES

In the previous section, Figs. 5.10–5.13 show that the $\overline{R}^{\lambda}$ balances are characterized by a large degree of cancellation between mean cell and eddy effects at times, while at other times, transports by mean cell and eddies operate nearly independently of one another. It is of considerable interest to examine these simulated phenomena in the context of some simplified theoretical results on disturbances in the stratosphere.

The work of Eliassen and Palm (1960) and Charney and Drazin (1961) [as later progressively generalized by Dickinson (1969), Holton (1974), Boyd (1976) and

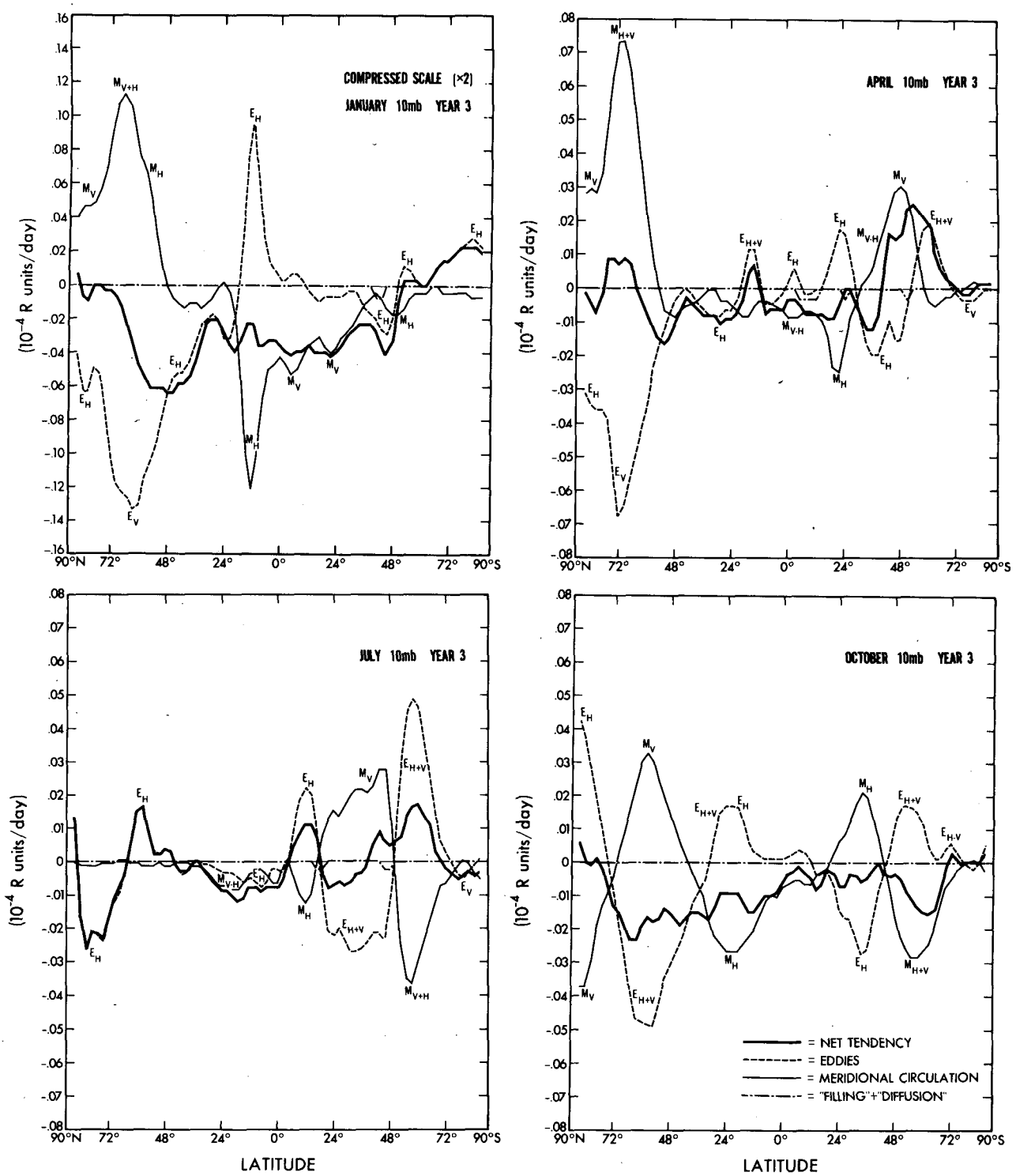

FIG. 5.13. As in Fig. 5.10 except at 10 mb, year 3. Note for July in northern latitudes the pronounced superposition of the eddies and net tendency.

Andrews and McIntyre (1976a,b)] show that, under many circumstances, eddies propagating to the stratosphere do not affect the zonal mean flow. Rather, they act to induce a meridional circulation which exactly cancels the eddy effect on the zonal flow. However, the validity of the non-interaction theorems are dependent upon the flow being nearly non-dissipative, adiabatic, steady (or harmonic time dependent) and of small

amplitude, as well as being away from the presence of singular lines (i.e., where the disturbance phase speed equals $\bar{u}^{\lambda}$). Under these assumptions, potential temperature and a well-stratified inert tracer become nearly equivalent quantities. Thus, a $\bar{T}^{\lambda}$ field unaltered by the presence of eddies carries similar implications for the $\bar{R}^{\lambda}$ field. When the above restrictions are not satisfied, the eddies must influence the zonal mean structure to some degree. What should be established, then, is the relative importance of these processes in producing departures from such idealized behavior in the real atmosphere. The GCM reported here should be quite useful for providing insight into such questions because the model equations allow a departure from all of the idealized conditions listed above.

Interpreted loosely, the non-interaction theorems would suggest that eddy disturbances from the troposphere exhibit only a weak influence on determining $\bar{u}^{\lambda}$ and $\bar{T}^{\lambda}$ in the stratosphere. If this were the case, the zonal mean fields would look very much like those determined by a radiative-symmetric equilibrium stratosphere. This is clearly *not* the case in the lower stratosphere winter season where the midlatitude warm belt is such a dominant feature. The departures are so marked that the zonal flow must be considered to be influenced significantly by the presence of eddies.

However, it is quite possible that these non-interaction theorems can be approximately valid locally and still have the zonal flow influenced to a significant degree by the eddy structure. For example, if the eddy forcing is large compared to the other processes acting to influence the zonal flow (such as diabatic heating), then a large degree of cancellation between mean cell and eddy transports would be expected even when the eddies are exerting a systematic effect on the zonal mean structure.

As an example of the role of eddy forcing, it is instructive to look at some aspects of the zonal mean balances in Northern Hemisphere January and July for high latitudes. It is in this region where Fig. 5.12 shows marked contrast in the tracer behavior for winter and summer months. A revealing way to examine this question is to look at the dominant terms in the high-latitude 65 mb heat balances for the two cases in Table 3.

It is interesting that the large eddy flux convergence in January is mostly compensated by the adiabatic compression term. Thus, most of the induced poleward eddy flux (resulting from upward eddy pressure interaction) leads to the well known winter indirect meridional circulation, while part of it is lost by radiative damping and essentially none is being used to change $\bar{T}^{\lambda}$. This is in marked contrast to the July balances where the eddy heat flux convergence is much smaller. In that case the meridional circulation effect is negligibly small, while $\bar{T}^{\lambda}$ is actually increasing in response to this weak eddy flux convergence. At first this seems surprising because the diabatic term is also small relative to the January value. However, the model July 65 mb high-latitude region is near the point of reversal between zonal mean westerlies and easterlies (MM76). This probably leads to a singular-line type effect for stationary and slowly moving waves, and thus leads to irreversible transport and alteration of the zonal mean structure as suggested by Dickinson (1969).

TABLE 3. Approximate zonal mean heat balance contributions at 65 mb for the region north of 60°N (°C day^{-1}). Smaller terms not shown.

	$\frac{\partial \bar{T}^{\lambda}}{\partial t} \approx$	$-\frac{1}{a\cos\phi}\frac{\partial}{\partial\phi}\overline{v'T'}^{\lambda}\cos\phi$	$+\bar{\omega}^{\lambda}\left(\frac{\bar{\alpha}^{\lambda}}{c_p}\right)$	$-\bar{\omega}^{\lambda}\left(\frac{\partial \bar{T}^{\lambda}}{\partial p}\right)+\frac{\bar{Q}^{\lambda}}{c_p}$
Jan.	small $\approx$	+1.4	−1.0	−0.4
Jul.	+0.1 $\approx$	+0.2	small	−0.1

Additional support is given for this in Fig. 11 of Mahlman (1973b) which shows the 65 mb flow field for 31 July in this experiment. That picture reveals a situation where the flow field is very weak, but the indicated meridional excursions of individual trajectories are very large as should be expected kinematically in a region where $\bar{u}^{\lambda} \to 0$ (e.g., see Haltiner and Martin, 1957, p. 185). Thus, almost paradoxically, the presence of eddies which are effective in producing changes in the zonal mean meteorological or tracer structure occurs at a time when the eddies themselves are quite weak.

For problems involving large apparent cancellation between mean cell and eddy effects, various authors have found the Lagrangian viewpoint to be illuminating (e.g., Riehl and Fultz, 1957; Mahlman, 1966, 1969a, 1973a; MM76; Andrews and McIntyre, 1976a; Kida, 1977b). In addition, the important role of transient disturbances is addressed by Matsuno (1971) and by Holton and Dunkerton (1978), among others. Both of these points will be discussed in greater detail in the tracer paper to follow this one.

c. *Tracer behavior in the troposphere*

1) CROSS-TROPOPAUSE TRANSPORT, THE MIDLATITUDE PEAK AND THE SPRING PEAK

As mentioned in the Introduction, tracer transport across the tropopause has been viewed as being dominated by either meridional circulation effects or by eddy processes. In this experiment, for the global mean $[\overline{(\ )}^{G}]$ vertical transports across the tropopause, the eddy transport $(\overline{\omega' R'}^{\lambda G})$ is approximately an order of magnitude larger than mean transport $(\overline{\bar{\omega}^{\lambda}\bar{R}^{\lambda}}^{G})$.

However, at a given latitude, the two effects tend to be of similar magnitude. This arises because the eddy flux is predominantly downward, while the mean flux alternates in sign depending upon the local sense of $\bar{\omega}^{\lambda}$.

The calculated strongest downward eddy cross-tropopause fluxes occur near 50–60°N during March–May. A similar result was obtained by Kida (1977a,b). This flux is predominantly associated with developing extratropical cyclones in a manner similar to that in the actual atmosphere as described in the introduction. A significant difference, however, is that the size of the region of descending air in individual disturbances is larger than observed. This is presumably a limitation of the current model resolution. A more detailed examination of this important process will appear in a future paper.

The strongest downward zonal mean fluxes occur near 35–45°N during December–February. These combined effects act to produce a simulated broad maximum of tracer mixing ratio in midlatitudes. This is in qualitative agreement with observation, but the observed values (e.g., U.S. Public Health Service Radiation Surveillance Network Data, 1967) appear to exhibit a somewhat sharper midlatitude maximum than obtained here. The probable cause for this qualitative difference is that the downward flux by the meridional circulation appears to be overestimated in the region near 30–35°N. This bias is even more pronounced in the predecesser experiment by Hunt and Manabe (1968), and also in Kao *et al.* (1976). It appears to be related to insufficient horizontal grid resolution in the GCM.

As mentioned in the Introduction, stratospheric radioactive tracers exhibit strong seasonal variations near the surface with a maximum in spring and a minimum in late fall in the Northern Hemisphere. It is thus of special interest to examine the behavior of this experiment in that regard. Fig. 5.14 is a plot of $\bar{R}^{\lambda}$ at 990 mb against time for latitudes 36, 48 and 60°N. Included for comparison purposes is the average gross beta activity in air over the U.S. Public Health Service Radiation Surveillance Network Data (1967) for the moratorium years of 1963 and 1964. The simulation shows a marked tendency for a spring maximum the first year. During the second year, the spring peak is only evident at 48° and 60°N. Relative to observation, the magnitude of the simulated seasonal variation is too small. In particular, the late fall minimum has been underestimated.

Although it is difficult to establish the actual causes for these differences, some important observations can be made. In this simulation, the spring peak is attributable to the action of the winter circulation producing a tracer buildup in the lower stratosphere. This process appears similar to that of the actual atmosphere. However, a defect of this model is that the spontaneous mid- and late-winter breakdowns (sudden warmings) have not been simulated (MM76). This probably leads to a

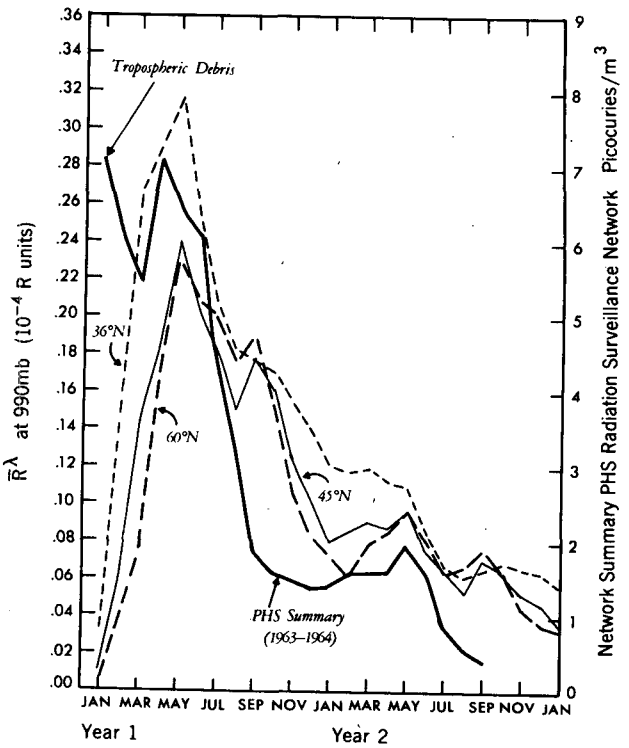

FIG. 5.14. Zonal mean tracer at 990 mb for indicated months and indicated latitudes (10^{-4} R units, at left). Heavy solid line is from U.S. Public Health Service, Radiation Surveillance Network (1967) for 1963 and 1964 following U.S.–U.S.S.R. test series of late 1962. Observed data are for contiguous U.S. area with values (pCi m^{-3}) given at right.

deficiency in the amount of tracer available in the model lower stratosphere during late winter. This same GCM defect leads to a delay in the onset of the summertime easterlies, and may be responsible for the easterlies being somewhat weaker, smaller in extent, and of shorter duration than observed. In turn, this probably leads to a simulated summertime transport efficiency greater than observed, thus obscuring the fall minimum, which appears to depend upon a weak summertime transport rate.

Another feature in Fig. 5.14 for which there is no observational counterpart is the increase in tracer amount from August to September. Although this model increase has no satisfactory explanation, it may be due to the use of a single year of GCM winds with a "recycling" jump at 1 August. As pointed out in MM76, the climatic structures across this jump are somewhat different and may have led to this behavior.

2) ZONAL MEAN BALANCES IN THE LOWER TROPOSPHERE

Once tracer is brought downward into the troposphere from the stratosphere, it is of considerable interest to view its behavior as it is influenced by a number of competing processes. Because of this, it is again convenient to view the zonal mean balances, but this time

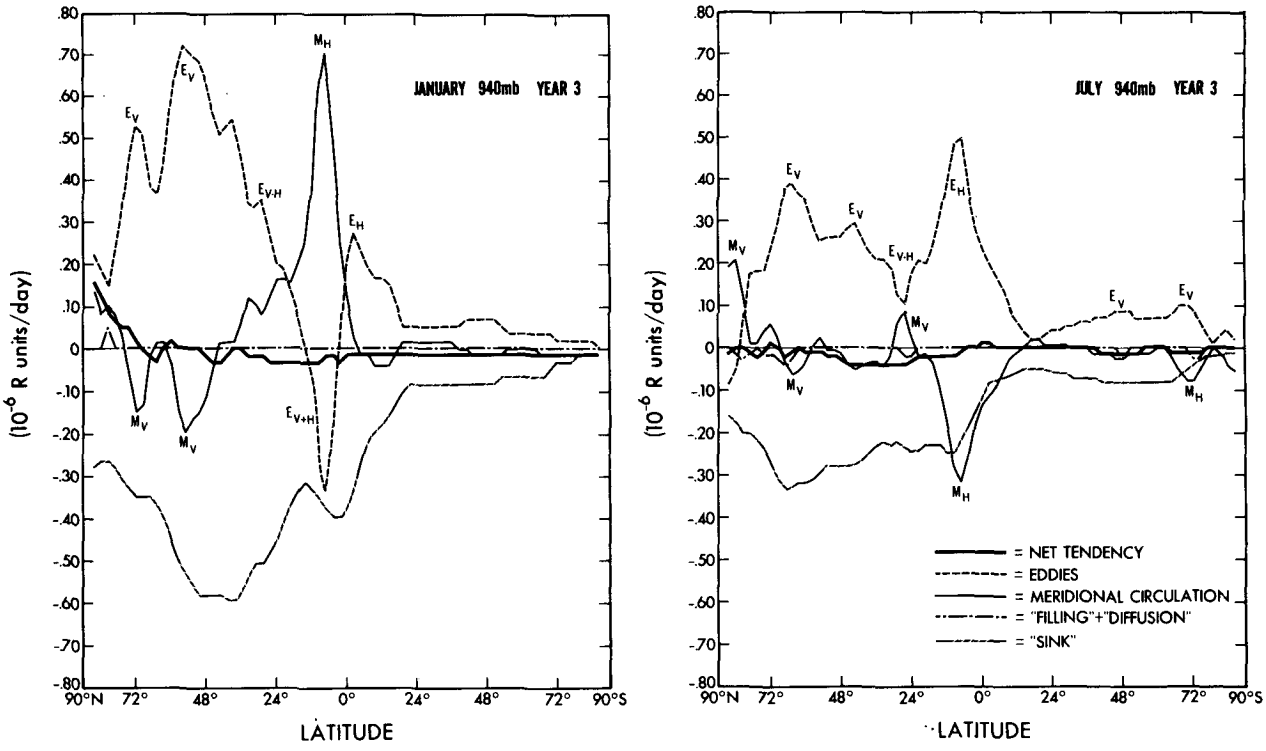

FIG. 5.15. As in Fig. 5.10 except at 940 mb, year 3 (10^{-6} R units day^{-1}).

in the lower troposphere where tracer destruction is an important effect.

Fig. 5.15 shows the $\overline{R}^{\lambda}$ balances at 940 mb for January and July during the third year of the experiment. The January balances show that most of the lower tropospheric tracer is supplied by downward eddy flux in midlatitudes. Most of this amount brought down is removed locally by the model rainfall-dependent removal mechanism. The remainder is moved through the subtropics by the horizontal component of the meridional circulation (M_H) (see MM76, Fig. 5.1). Once into the tropics, it is moved into the model intertropical convergence zone (ITCZ) by convergence of horizontal eddy tracer flux (E_H). This is then balanced by an efficient tracer removal due to the significant model precipitation there (Manabe *et al.*, 1974).

For July, Fig. 5.15 shows again a large effect due to downward eddy flux in midlatitudes. Note the shift toward higher northern latitudes compared with the January balances. This is consistent with the summer shift of the maximum cyclonic activity toward higher latitudes (see MM76, Fig. 6.1). In the subtropics, the tracer is moved equatorward by horizontal eddies leading to a large buildup in the ITCZ (E_H positive). During July this equatorial flux convergence is opposed by evacuation through the meridional circulation (M_H) which is moving poleward in the surface layers. The net effect, however, is to import a substantial amount of tracer into the ITCZ for removal there.

Finally, it is of interest to note that the lower troposphere tracer structure is typified by the total flux divergence being balanced locally by destruction, while the local time rate of change of $\overline{R}^{\lambda}$ is significantly smaller than either of these processes.

6. Summary

a. Comparison with observations

The four-year evolution of this numerical simulation of a midlatitude instantaneous release of tracer shows many features which agree with observed tracer structure: the average poleward-downward slopes of the mixing ratio contours; the strong gradients across the tropopause; the pronounced protrusion of tracer across the equator into the Southern Hemisphere lower stratosphere; and the long-term interhemispheric exchange rate.

The model produces the largest transport to the troposphere through the midlatitude cyclones, in agreement with observation. A spring maximum and fall minimum in surface values is simulated, but with an amplitude significantly smaller than observed. This deficiency is apparently related to the inability of the model to simulate midwinter sudden stratospheric warming episodes and their subsequent effect on the onset of the summertime circulation.

The calculated global residence time of the model exhibits behavior which falls between those observed

for particulate tracers and for gaseous $C^{14}O_2$. In the early months of the experiment, the model residence time is less than one year, while it increases to greater than two years by the end of the experiment. This result appears quite consistent with observed residence times in the sense that the experimental design does not include particulate settling (similar to $C^{14}O_2$), but does incorporate efficient tropospheric removal processes (similar to particulate tracers). These results lead to the inference that settling is quite important at longer times for particulate tracers. On the other hand, back transfer of $C^{14}O_2$ from the troposphere at longer times appears to significantly affect its apparent stratospheric residence time.

The intermediate character of this experiment suggests a hazard involved in indiscriminate use of either observed $C^{14}O_2$ or particulate debris data for calibration of general empirical transport models. If such models were to be applied to the problem of dispersion of gaseous anthropogenic tracers in the stratosphere which are strongly removed in the troposphere (e.g., odd nitrogen, odd chlorine or H_2O), they could yield either overestimates or underestimates of the net stratospheric transport rate, depending on which data source is used.

An additional inference is that the stratospheric residence time is a rather strong function of the elevation of the average center of mass of the tracer. According to this model, the mean residence time tends to increase by about 0.3–0.4 year for each kilometer rise in tracer center of mass.

b. *Dynamical interpretations*

An intriguing result of this experiment is that initially low tracer/potential vorticity correlations grow to moderately high values in a month, while becoming very large within a half year. The short-term growth appears to be related to the specific manner in which eddy energy conversions are effected in the model stratosphere. The growth of correlation at longer time scales is related to the time required for the relative vertical tracer stratification to be similar to the average vertical stratification of potential vorticity.

The zonal mean tracer balances are shown to be a complex combination of horizontal and vertical processes in both mean and eddy terms. In the early stages, however, eddy processes are the dominant dispersion mechanism. Later, in agreement with earlier results, a very high degree of cancellation between mean cell and eddy transports is observed in the midwinter balances.

A new result is that this cancellation effect disappears dramatically at seasonal transitions in the stratospheric circulation. During these decouplings, the zonal mean tracer is altered by the eddies at a time when the eddies themselves are quite weak. This phenomenon appears to be related to the efficiency of the mechanical eddy forcing of the stratosphere relative to the magnitude of opposing radiative effects. It appears to be augmented by the presence of a singular-line type transition between zonal westerlies and easterlies during the summer season.

Acknowledgments. The authors are deeply grateful to Dr. S. Manabe who designed the GCM, formulated the original tracer model concept, and contributed many valuable insights. Appreciation is due to Dr. J. Smagorinsky whose efforts make it possible to give this kind of research the extended commitment it requires.

This work was critically dependent upon the efforts of J. L. Holloway, Jr., D. G. Hahn and D. Daniel, who were instrumental in various phases of the work on the GCM. The work of S. Kenety and E. Thompson in manuscript preparation is gratefully acknowledged. Thanks are due to Drs. S. Manabe, H. Levy II, J. R. Holton and W. B. Rossow for their helpful criticisms of the manuscript.

In a project of this scope, one is dependent upon the efforts of a great number of persons. The results presented here depend to a great extent upon the support given by the GFDL administration, technical staff, systems analysts, computer operators, and numerous scientific colleagues.

Early portions of this work were supported by the Division of Biology and Medicine, U.S. Atomic Energy Commission.

REFERENCES

Andrews, D. G., and M. E. McIntyre, 1976a: Planetary waves in horizontal and vertical shear: The generalized Eliassen-Palm relation and the mean zonal acceleration. *J. Atmos. Sci.*, **33**, 2031–2048.

——, 1976b: Planetary waves in horizontal and vertical shear: An asymptotic theory for equatorial waves in weak shear. *J. Atmos. Sci.*, **33**, 2049–2053.

Boyd, J. P., 1976: The noninteraction of waves with the zonally averaged flow on a spherical earth and the interrelationships of eddy fluxes of energy, heat and momentum. *J. Atmos. Sci.*, **33**, 2285–2291.

Boville, B. W., and F. K. Hare, 1961: Total ozone and perturbations in the middle stratosphere. *Quart. J. Roy. Meteor. Soc.*, **87**, 490–501.

Brewer, A. W., 1949: Evidence for a world circulation provided by measurement of helium and water vapor distribution in the stratosphere. *Quart. J. Roy. Meteor. Soc.*, **75**, 351–363.

Bryan, K., 1966: A scheme for numerical integration of the equations of motion on an irregular grid free of nonlinear instability. *Mon. Wea. Rev.*, **94**, 39–40.

Chang, J. S., 1976: Uncertainties in the validation of parameterized transport in 1-D models of the stratosphere. *Proc. Fourth Conf. Climatic Impact Assessment Program*, T. M. Hard and A. J. Broderick, Eds., 175–182 [DOT-TSC-OST-75-38].

Charney, J. G., and P. G. Drazin, 1961: Propagation of planetary-scale disturbances from the lower into the upper atmosphere. *J. Geophys. Res.*, **66**, 83–109.

Craig, R. A., 1950: *The Observations and Photochemistry of Atmospheric Ozone and their Meteorological Significance. Meteor. Monogr.*, No. 2, Amer. Meteor. Soc., 50 pp.

Cunnold, D., F. Alyea, N. Phillips and R. Prinn, 1975: A three-dimensional dynamical-chemical model of atmospheric ozone. *J. Atmos. Sci.*, **32**, 170–194.

Danielsen, E. F., 1959a: A determination of the mass transported from stratosphere to troposphere over North America over a thirty-six hour interval (Abstract). *Milt. Dtsch. Wetter.*, **20**, 10–11.

——, 1959b: The laminar structure of the atmosphere and its relation to the concept of a tropopause. *Arch. Meteor. Geophys. Bioklim.*, **A11**, 293–332.

——, 1964: Radioactivity transport from stratosphere to troposphere. *Mineral Ind.*, **33**, 1–7.

——, 1968: Stratospheric-tropospheric exchange based on radioactivity, ozone and potential vorticity. *J. Atmos. Sci.*, **25**, 502–518.

——, R. Bleck, J. Shedlovsky, A. Wartburg, P. Haagenson and W. Pollock, 1970: Observed distribution of radioactivity, ozone, and potential vorticity associated with tropopause folding. *J. Geophys. Res.*, **75**, 2353–2361.

Deardorff, J. W., 1971: On the magnitude of the subgrid-scale eddy coefficient. *J. Comput. Phys.*, **7**, 120–133.

Dickinson, R. E., 1969: Theory of planetary wave-zonal flow interaction. *J. Atmos. Sci.*, **26**, 73–81.

Dobson, G. M. B., 1956: Origin and distribution of polyatomic molecules in the atmosphere. *Proc. Roy. Soc. London*, **A236**, 187–193.

Eliassen, A., and E. Palm, 1960: On the transfer of energy in stationary mountain waves. *Geophys. Publ.*, **22**, 1–23.

Fabian, P., and W. F. Libby, 1974: The stratospheric residence time of odd nitrogen and the effect of the SST studied in a two-dimensional model derived from high-altitude sampling of radioactive debris. *Proc. Third Conf. Climatic Impact Assessment Program*, A. J. Broderick and T. M. Hard, Eds. 103–116 [DOT-TSC-OST-74-15].

Feely, H. W., and J. Spar, 1960: Tungsten-185 from nuclear bomb tests as a tracer for stratospheric meteorology. *Nature*, **188**, 1062–1064.

——, H. Seitz, R. J. Lagomarsino and P. E. Biscayne, 1966: Transport and fallout of stratospheric radioactive debris. *Tellus*, **18**, 316–328.

Godson, W. L., 1960: Total ozone and the middle stratosphere over arctic and sub-arctic areas in winter and spring. *Quart. J. Roy. Meteor. Soc.*, **86**, 301–317.

Goldie, A. H. R., 1958: The average planetary circulation in vertical meridian planes. *Proc. Roy. Soc. London*, **A238**, 175–180.

Hahn, D. G., and S. Manabe, 1975: The role of mountains in the South Asian monsoon circulation. *J. Atmos. Sci.*, **32**, 1515–1541.

Haltiner, G. J., and F. L. Martin, 1957: *Dynamical and Physical Meteorology*. McGraw-Hill, 470 pp.

Hartmann, D. L., 1977: On potential vorticity and transport in the stratosphere. *J. Atmos. Sci.*, **34**, 968–977.

Hayashi, Y., 1974: Spectral analysis of tropical disturbances appearing in a GFDL general circulation model. *J. Atmos. Sci.*, **31**, 180–218.

——, and D. G. Golder, 1977: Space-time spectral analysis of mid-latitude disturbances appearing in a GFDL general circulation model. *J. Atmos. Sci.*, **34**, 237–262.

Hering, W. S., 1965: Ozone and atmospheric transport processes. *Tellus*, **18**, 329–336.

——, and T. R. Borden, 1964: Ozonesonde observations over North America. U.S. Air Force Cambridge Research Laboratories, Environ. Res. Pap., No. 38, Vol. 2, 280 pp. [NTIS No. AD 604 880].

Holloway, J. L., Jr., and S. Manabe, 1971: Simulation of climate by a global general circulation model. I. Hydrologic cycle and heat balance. *Mon. Wea. Rev.*, **99**, 335–370.

Holton, J. R., 1974: Forcing of mean flows by stationary waves. *J. Atmos. Sci.*, **31**, 942–945.

——, and T. Dunkerton, 1978: On the role of wave transience and dissipation in stratospheric mean flow vacillations. *J. Atmos. Sci.*, **35**, 740–744.

Hoskins, B. J., 1971: Atmospheric frontogenesis models: Some solutions. *Quart. J. Roy. Meteor. Soc.*, **97**, 139–153.

Hunt, B. G., 1969: Experiments with a stratospheric general circulation model. III. Large-scale diffusion of ozone including photochemistry. *Mon. Wea. Rev.*, **97**, 287–306.

——, and S. Manabe, 1968: Experiments with a stratospheric general circulation model. II. Large-scale diffusion of tracers in the stratosphere. *Mon. Wea. Rev.*, **96**, 503–539.

Hunten, D. M., 1975: Residence times of aerosols and gases in the stratosphere. *Geophys. Res. Lett.*, **2**, 26–28.

Johnston, H. S., D. Kattenhorn and G. Whitten, 1976: Use of excess carbon-14 data to calibrate models of stratospheric ozone depletion by supersonic transports. *Proc. Fourth Conf. Climatic Impact Assessment Program*, T. M. Hard and A. J. Broderick, Eds. 156–174 [DOT-TSC-OST-75-38].

Julian, P. R., and K. B. Labitzke, 1965: A study of atmospheric energetics during the January-February 1963 stratospheric warming. *J. Atmos. Sci.*, **22**, 597–610.

Junge, C. E., C. W. Chagnon and J. E. Mason, 1961: Stratospheric aerosols. *J. Meteor.*, **18**, 81–108.

Kao, S. K., C. N. Chi and W. M. Washington, 1976: Statistical characteristics of three-dimensional particle movement in the NCAR general circulation model. *J. Atmos. Sci.*, **33**, 1042–1049.

Kida, H., 1977a: A numerical investigation of the atmospheric general circulation and stratospheric tropospheric mass exchange. I. Long term integration of a simplified general circulation model. *J. Meteor. Soc. Japan*, **55**, 52–70.

——, 1977b: A numerical investigation of the atmospheric general circulation and stratospheric tropospheric mass exchange. II. Lagrangian motion of the atmosphere. *J. Meteor. Soc. Japan*, **55**, 71–88.

Krishnamurti, T. N., 1961a: The subtropical jet stream of winter. *J. Meteor.*, **18**, 172–191.

——, 1961b: On the role of the subtropical jet stream of winter in the atmospheric general circulation. *J. Meteor.*, **18**, 657–670.

Kurihara, Y., and J. L. Holloway, Jr., 1967: Numerical integration of a nine-level global primitive equations model formulated by the box method. *Mon. Wea. Rev.*, **95**, 509–530.

Libby, W. F., and C. E. Palmer, 1960: Stratospheric mixing from radioactive fallout. *J. Geophys. Res.*, **65**, 3307–3317.

Lilly, D. K., D. E. Waco and S. I. Adelfang, 1974: Stratospheric mixing estimated from high altitude turbulence measurements. *J. Appl. Meteor.*, **13**, 488–493.

Machta, L., and K. Telegadas, 1973: Examples of stratospheric transport. *Proc. Second Conf. Climatic Impact Assessment Program*, A. J. Broderick, Ed., 47-56 [DOT-TSC-OSC-73-4].

Mahlman, J. D., 1965: Relation of stratospheric-tropospheric mass exchange mechanisms to surface radioactivity peaks. *Arch. Meteor. Geophys. Bioklim.*, **A15**, 1–25.

——, 1966: Atmospheric general circulation and transport of radioactive debris. Atmospheric Science Paper No. 103, Colorado State University, 184 pp.

——, 1969a: Heat balance and mean meridional circulations in the polar stratosphere during the sudden warming of January 1958. *Mon. Wea. Rev.*, **97**, 534–540.

——, 1969b: Long-term dependence of surface fallout fluctuations upon tropopause-level cyclogenesis. *Arch. Meteor. Geophys. Bioklim.*, **A18**, 299–311.

——, 1973a: On the maintenance of the polar front jet stream. *J. Atmos. Sci.*, **30**, 544–557.

——, 1973b: Preliminary results from a three-dimensional general-circulation/tracer model. *Proc. Second Conf. Climatic Impact Assessment Program*, A. J. Broderick, Ed., 321–337 [DOT-TSC-OST-73-4].

——, and W. J. Moxim, 1976: A method for calculating more accurate budget analyses of "sigma" coordinate model results. *Mon. Wea. Rev.*, **104**, 1102–1106.

——, and R. W. Sinclair, 1977: Tests of various numerical algorithms applied to a simple trace constituent air transport problem. *Fate of Pollutants in the Air and Water Environments*, Part 1, Vol. 8 of *Advances in Environmental Science and Technology*, I. H. Suffet, Ed., Wiley, 223–252.

Manabe, S., and R. F. Strickler, 1964: Thermal equilibrium of the atmosphere with a convective adjustment. *J. Atmos. Sci.*, **21**, 361–385.

——, J. Smagorinsky, and R. F. Strickler, 1965: Simulated climatology of a general circulation model with a hydrologic cycle. *Mon. Wea. Rev.*, **93**, 769–798.

——, and R. T. Wetherald, 1967: Thermal equilibrium of the atmosphere with a given distribution of relative humidity. *J. Atmos. Sci.*, **24**, 241–259.

——, and B. G. Hunt, 1968: Experiments with a stratospheric general circulation model. I. Radiative and dynamic aspects. *Mon. Wea. Rev.*, **96**, 477–502.

——, and J. L. Holloway, Jr., 1975: The seasonal variation of the hydrologic cycle as simulated by a global model of the atmosphere. *J. Geophys. Res.*, **80**, 1617–1649.

——, and J. D. Mahlman, 1976: Simulation of seasonal and interhemispheric variations in the stratospheric circulation. *J. Atmos. Sci.*, **33**, 2185–2217.

——, D. G. Hahn and J. L. Holloway, Jr., 1974: The seasonal variation of the tropical circulation as simulated by a global model of the atmosphere. *J. Atmos. Sci.*, **31**, 43–83.

Matsuno, T., 1971: A dynamical model of the stratospheric sudden warming. *J. Atmos. Sci.*, **28**, 1479–1494.

Miyakoda, K., R. F. Strickler, C. J. Nappo, P. L. Baker and G. D. Hembree, 1971: The effect of horizontal grid resolution in an atmospheric circulation model. *J. Atmos. Sci.*, **28**, 481–499.

Mudrick, S. E., 1974: A numerical study of frontogenesis. *J. Atmos. Sci.*, **31**, 869–892.

Murakami, T., 1965: Energy cycle of the stratospheric warming in early 1958. *J. Meteor. Soc. Japan*, Ser. 2, **43**, 262–283.

Newell, R. E., 1961: The transport of trace substances in the atmosphere and their implications for the general circulation of the stratosphere. *Geofis. Pura Appl.*, **49**, 137–158.

——, 1963: The general circulation of the atmosphere and its effects on the movement of trace substances. *J. Geophys. Res.*, **68**, 3949–3962.

Phillips, N. A., 1957: A coordinate system having some special advantages for numerical forecasting. *J. Meteor.*, **14**, 184–185.

Ramanathan, K. R., and R. N. Kulkarni, 1960: Mean meridional distributions of ozone in different seasons calculated from umkehr observations and probable vertical transport mechanisms. *Quart. J. Roy. Meteor. Soc.*, **86**, 144–155.

Reed, R. J., 1953: Large-scale eddy flux as a mechanism for vertical transport of ozone. *J. Meteor.*, **10**, 296–297.

——, 1955: A study of a characteristic type of upper-level frontogenesis. *J. Meteor.*, **12**, 226–237.

——, and A. L. Julius, 1951: A quantitative analysis of two proposed mechanisms for vertical ozone transport in the lower stratosphere. *J. Meteor.*, **8**, 321–325.

——, and F. Sanders, 1953: An investigation of the development of a mid-tropospheric frontal zone and its associated vorticity field. *J. Meteor.*, **10**, 338–349.

——, and E. F. Danielsen, 1959: Fronts in the vicinity of the tropopause. *Arch. Meteor. Geophys. Bioklim.*, **A11**, 1–17.

——, J. L. Wolfe and H. Nishimoto, 1963: A spectral analysis of the energetics of the stratospheric sudden warming of early 1957. *J. Atmos. Sci.*, **20**, 256–275.

Reiter, E. R., 1963: A case study of radioactive fallout. *J. Appl. Meteor.*, **2**, 691–705.

——, and J. D. Mahlman, 1965: Heavy radioactive fallout over the southern United States, November 1962. *J. Geophys. Res.*, **70**, 4501–4520.

Riehl, H., and D. Fultz, 1957: Jet stream and long waves in a steady rotating-dishpan experiment: Structure of the circulation. *Quart. J. Roy. Meteor. Soc.*, **83**, 215–231.

Smagorinsky, J., 1963: General circulation experiments with the primitive equations. I. The basic experiment. *Mon. Wea. Rev.*, **91**, 99–164.

Staley, D. O., 1960: Evaluation of potential-vorticity changes near the tropopause and the related vertical motions, vertical advection of vorticity, and transport of radioactive debris from stratosphere to troposphere. *J. Meteor.*, **17**, 591–620.

——, 1962: On the mechanism of mass and radioactivity transport from stratosphere to troposphere. *J. Atmos. Sci.*, **19**, 450–467.

Telegadas, K., 1971: The seasonal atmospheric distribution and inventories of excess carbon-14 from March 1955 to July 1969. Health and Safety Laboratory, Fallout Program Quart. Summary Rep., HASL-243, 1-87.

——, and R. J. List, 1969: Are particulate radioactive tracers indicative of stratospheric motions? *J. Geophys. Res.*, **74**, 1339–1350.

U.S. Public Health Service, 1967: Radiation Surveillance Network, monthly averages of gross beta radioactivity in air in the Western Hemisphere—September 1961 through December 1966. National Center for Radiological Health, 85 pp.